A two-step inversion approach for seismic-reservoir characterization and a comparison with a single-loop Markov-Chain Monte Carlo algorithm

Mattia Aleardi*, Fabio Ciabarri°, Timor Gukov°

*University of Pisa, Earth Sciences Department, °Edison

Corresponding author: Mattia Aleardi, mattia.aleardi@unipi.it

Abstract

We describe a two-step Bayesian algorithm for seismic-reservoir characterization, which, thanks to some simplifying assumptions, is computationally very efficient. The applicability and reliability of this method are assessed by comparison with a more sophisticated and computer intensive Markov Chain Monte Carlo (MCMC) algorithm, which in a single-loop directly estimates petrophysical properties and litho-fluid facies from pre-stack data. The two-step method first combines a linear rock-physics model with the analytical solution of a linearized amplitude versus angle (AVA) inversion, to directly estimate petrophysical properties, and related uncertainties, from pre-stack data under the assumptions of a Gaussian prior model and weak contrasts at the reflecting interface. In particular, we use an empirical, linear rock-physics model, properly calibrated for the investigated area, to reparametrize the linear time-continuous P-wave reflectivity equation in terms of petrophysical contrasts instead of elastic constants. In the second step, a downward 1-D Markov chain prior model is used to infer the litho-fluid classes from the outcomes of the first step. The single-loop MCMC algorithm uses a convolutional forward modelling based on the exact Zoeppritz equations, and adopts a non-linear rock-physics model. Moreover, it assumes a more realistic Gaussian mixture distribution for the petrophysical properties. Both approaches are applied on an onshore 3-D seismic dataset for the characterization of a gas-bearing, clastic reservoir. Notwithstanding the differences in the forward-model parameterization, in the considered rock-physics model, and in the assumed a-priori probability density functions, the two methods yield

maximum a-posteriori solutions that are consistent with well log data, although the Gaussian mixture assumption adopted by the single-loop method slightly improves the description of the multimodal behavior of the petrophysical parameters. However, in the considered reservoir, the main difference between the two approaches remains the very different computational times, being the single-loop method much more computationally intensive than the two-step approach.

Introduction

Three-dimensional (3-D) numerical reservoir models play a key role in the exploration and production industry, as they describe the spatial variability of reservoir properties (i.e. porosity, water saturation, shale content) and litho-fluid facies around the target zone. However, due to sparse well coverage, reservoir models are often poorly constrained away from well locations. Therefore, a key challenge for reservoir geoscientists is the quantitative integration of 3-D seismic data to obtain a more accurate representation of the reservoir characteristics between the wells (Doyen, 2007). To this aim, recent efforts have been focused in developing inversion algorithms for seismic-reservoir characterization that reliably estimate rock properties and litho-fluid facies from pre-stack seismic data (Avseth et al. 2005; Bosch et al., 2010). However, it is known that seismic data do not provide direct information about reservoir properties or litho-fluid facies, but instead reflect the elastic contrasts in the subsurface (i.e. the contrasts in P-wave velocity, *Vp*; S-wave velocity, *Vs*, and density, ρ). For this reason, seismic-reservoir characterization is usually a multi-step procedure: first elastic parameters are estimated from seismic data by means of an inversion procedure that can be tackled using high computer intensive strategies, such as full-waveform inversion (Bachrach et al. 2004; Sajeva et al. 2016; Aleardi et al. 2016; Aleardi and Mazzotti 2017), or adopting methods that are less computationally demanding, such as the amplitude versus angle (AVA) approach (Buland and Omre 2003; Mazzotti and Zamboni 2003; Veire et al. 2006; Skopintseva et al. 2012; Aleardi and Mazzotti, 2014; Aleardi et al. 2015; Aleardi and Tognarelli 2016). The step of petrophysical inversion that follows, uses a rock physics model (RPM) and the seismic attributes obtained from

elastic inversion, to estimate the petrophysical properties of interest, such as porosity, clay volume, and possibly fluid saturations. The RPM is a mathematical model that converts the petrophysical properties into the elastic properties, and it can be defined adopting both empirical or theoretical approaches (Mazzotti and Zamboni, 2003; Chiappa and Mazzotti, 2009; Mavko et al. 2009; Aleardi and Ciabarri 2017a). If needed a transfer function or a classification algorithm can be used to associate the petrophysical (or elastic) properties previously estimated to a given litho-fluid class (Aleardi and Ciabarri, 2017b).

As discussed in Doyen (2007), this multi-step approach often does not guarantee that the final petrophysical model is fully consistent with the seismic data, in that the seismic response computed from the earth model are not guaranteed to reproduce the observed seismic data. In other words, this multi-step approach gives not identical results to the approach in which reservoir properties are directly estimated from pre-stack data (Bosh, 2004). Another drawback of this multi-step approach concerns the error propagation from the data (seismic) space to the model (petrophysical) space, especially for non-linear inversions (Zunino et al. 2014; Li and Zhang, 2015). To circumvent these issues, the rock physics model and the facies classification can be integrated into the seismic inversion workflow. In this approach, usually referred to as single-loop inversion (Grana et al. 2012), a model of facies (or litho-fluid classes) is generated; the petrophysical properties are distributed into the facies model and successively the rock physics model is applied to generate the corresponding elastic properties. Then synthetic seismic traces are computed (i.e. by a convolutional model) and are compared to real seismic data to evaluate the mismatch; the procedure is iterated by modifying the current model until a satisfactory match between synthetic and observed seismic amplitudes is achieved. As an alternative to this computationally demanding method, a mathematical transformation can be used to directly link the sought petrophysical parameters to the seismic response. Once that this seismic-petrophysical transformation has been defined, it can be included into an inversion framework to directly estimate petrophysical properties from pre-stack data. As demonstrated in Mazzotti and Zamboni (2003) this petrophysical

reparameterization of the inversion kernel also helps reducing the range of admissible petrophysical solutions that is, the ambiguity of the seismic-petrophysical inverse problem.

Independently from the approach adopted, the estimation of reservoir properties from pre-stack seismic data is an ill-posed inverse problem, which means that the model parameters cannot be uniquely recovered. For this reason, this inverse problem is usually casted into a Bayesian framework (Tarantola, 2005; Aster et al. 2011; Fernandez Martinez et al. 2012). The final solution of a Bayesian inversion is the posterior probability density function (PDF), which expresses the probability of occurrence of model given the observed data. Two common assumptions in Bayesian inversion are a Gaussian prior PDF, and the linearity of the physical relation between the model and the data. These two assumptions are not necessary for solving the inverse problem, but make the analytical computation of the posterior PDF possible. Several physical models in geophysics are linear or can be locally linearized (i.e. convolutional model, acoustic and elastic wave-equations). But unfortunately, many properties in the subsurface, such as elastic attributes, or petrophysical properties are generally non-Gaussian, but exhibit a multimodal behavior related to the different fluid and rock properties of different litho-fluid classes (Grana and Della Rossa 2010; Sauvageau et al. 2014; Amaliksen 2014). Accounting for this multimodality can provide more reliable uncertainty estimations (Grana et al. 2017). In addition, rock-physics models are often nonlinear so that nonlinear optimization algorithms, such as gradient-based methods (i.e Gauss-Newton; steepest descent; Aster et al. 2011), or stochastic optimization algorithms (i.e. genetic algorithms, particle swarm, simulated annealing; Sajeva et al. 2017a) must be used to solve the inverse problem. From the one hand, gradient-based methods linearize the problem around an initial solution, losing the information necessary for a correct uncertainty appraisal. In addition, these methods are limited by their local nature; i.e., they terminate in the nearest minimum of the misfit function, which may not coincide with the global minimum. Despite these limitations, local methods are often applied for their limited computational cost (Chiappa and Mazzotti 2009; Aleardi et al. 2017a). On the other hand, stochastic optimization algorithms are less prone to get trapped into local minima, but

requires a computational cost that exponentially increases with the number of model parameters. In addition, these methods often give biased uncertainty estimations (Sen and Stoffa, 1996), although some strategies have been proposed to tackle this issue (Sambridge, 1999; Aleardi and Mazzotti, 2017; Sajeva et al. 2017b).

Otherwise, Markov Chain Monte Carlo (MCMC) methods (Sambridge and Moosegard 2002) are a class of sampling algorithms that can be used to numerically compute the posterior PDF (Sen and Stoffa, 1996; Eidsvik et al., 2004; Larsen et al., 2006; Gunning and Glinsky, 2007; Rimstad and Omre, 2010; Ulvmoen and Omre, 2010). In case of non-linear problems, MCMC methods provide some advantages over the gradient-based approach at the expense of an increased computational effort. First of all, MCMC methods can handle the nonlinearities of the inverse problem because only forward modeling and sampling of the prior PDF are needed to run the algorithm without the need to compute derivatives. Secondarily, MCMC algorithms efficiently explore the model space, so that several regions may be sampled. In addition, MCMC algorithms can be also used to sample non-parametric distributions. This results in a more comprehensive characterization of possible solutions, and a more robust estimation of uncertainties.

In this work, we present a fast, two-step (TS) approach for seismic-reservoir characterization in which we assume a Gaussian prior model, and linear relations between seismic and elastic attributes and between elastic attributes and petrophysical properties. First, a linear seismic-petrophysical forward operator is derived by combining a linear RPM (properly calibrated for the investigated area) and the linear time-continuous AVA equation for P-P reflectivity (Stolt and Weglein, 1985), which is valid for weak elastic contrasts at the reflecting interface and for a limited range of incidence angles (usually, 0-30 degrees). In the second step, the posterior PDF of litho-fluid facies is derived by combining the estimated petrophysical properties and associated uncertainties, with a downward Markov Chain prior model. Several authors (i.e. Buland and Omre, 2003; Alpak et al. 2006; Shahraeeni and Curtis, 2011; Bongajum et al. 2013; Jalalalhosseini et al. 2014; Grana 2016; Gong and McMechan, 2016; Grana et al. 2017; among many others) have implemented inversion

approaches that estimate elastic attributes from seismic data or convert elastic characteristics into petrophysical properties. Differently, in this work we use the seismic-petrophysical forward operator to integrate the elastic and the petrophysical inversions into a single inversion kernel for the analytical and direct estimation of petrophysical properties, and related uncertainties, from pre-stack data.

The TS method relies on three fundamental assumptions: a linear or almost linear rock-physics model, Gaussian-distributed model parameters, and weak contrasts at the reflecting interface. To analyses the effects of these assumptions on the estimated reservoir properties in the investigated area, we compare the predictions of the two-step method with those provided by a non-linear MCMC inversion in which the elastic inversion, the petrophysical inversion and the litho-fluid facies classification are integrated into a single-loop algorithm. Differently from the TS approach, this method (that we indicate with the acronym SL) more realistically assumes a Gaussian mixture prior model, so that the facies dependent behavior of petrophysical properties is taken into account. In addition, the SL algorithm adopts a theoretical, non-linear, RPM based on granular media models (Mavko et al. 2009; Avseth et al. 2005), and uses the exact Zoeppritz equations as the seismic forward modelling, thus relaxing the assumptions of a linear RPM and weak contrasts at the reflecting interface. Being the theoretical RPM and the exact Zoeppritz equations non-linear, the SL approach guarantees an accurate uncertainty propagation from the data to the model space. For both algorithms, we adopt a statistical approach to rock-physics modelling, in which the uncertainty related to the RPM definition is treated as a random variable and correctly propagated into the final predictions. The TS and SL approaches, overlook the lateral correlation of elastic, petrophysical properties and litho-fluid facies. Therefore, the lateral continuity of our results will be mainly related to the lateral correlation of seismic data that is dependent on the Fresnel zone and the associated migration operator. Conversely, the vertical correlation of petrophysical properties and litho-fluid facies are correctly taken into account by the two inversion algorithms. In particular, a stationary correlation function (Buland and Omre, 2003) is used to model the vertical correlation of

petrophysical properties, whereas a downward transition matrix is used to properly model the vertical succession of litho-fluid facies.

We start by introducing the theoretical aspects of the two inversion strategies. Then, we focus our attention on analyzing and validating the empirical, linear, rock-physic model. Finally, both synthetic data and field data inversions are used to compare the two methods. In the field data example, a blind test is also used to assess the prediction capability of the two methods and the reliability of the results.

Theoretical framework

We formulate the inversion a Bayesian setting, in which the final outcomes and their related uncertainties, are expressed using posterior probability density functions (PDFs; Tarantola, 2005). By considering l time samples, the vector **e** will refer to elastic properties (P-wave velocity, *Vp*, S-wave velocity *Vs*, and density ρ; $\mathbf{e}=[Vp_{1,\dots,l}, Vs_{1,\dots,l}, \rho_{1,\dots,l}]^T$), **m** indicates the natural logarithm of such properties ($\mathbf{m}=[\ln(Vp_{1,\dots,l}), \ln(Vs_{1,\dots,l}), \ln(\rho_{1,\dots,l})]^T$), **r** represents the petrophysical properties of interest (water saturation *Sw*; porosity φ; shaliness, *Sh*). The vector **d** indicates the observed seismic data (partially stacked data at different incidence angles), whereas **f** expresses the litho-fluid facies (shale, brine sand and gas sand).

The Bayesian approach and the Markov Chain Monte Carlo methods

In a Bayesian inversion, the posterior PDF can be derived as (Tarantola, 2005):

$$p(\mathbf{k} \mid \mathbf{d}) = p(\mathbf{d} \mid \mathbf{k})\, p(\mathbf{k}) / p(\mathbf{d}) \qquad (1)$$

where **k** represents the vector of model parameters, the symbol $p()$ indicates a probability density function, and the pipe symbol | indicates a conditional dependence. The probability $p(\mathbf{k}|\mathbf{d})$ is the target PDF, $p(\mathbf{k})$ is the prior PDF of model parameters, usually defined independently from the data **d**, and $p(\mathbf{d}|\mathbf{k})$ is the so-called likelihood function that expresses the probability of measuring the observed data **d** for a given model **k**. The denominator $p(\mathbf{d})$ is the prior PDF of data that is usually

considered a normalizing factor that makes the integral of $p(\mathbf{k}|\mathbf{d})$ over the model space equal to unity. A plain and exact analytical solution of equation 1 only exists in case of a linear inverse problem with Gaussian assumptions about the distributions of model parameters and data. In case of non-linear problems Markov Chain Monte Carlo methods can be used to derive a numerical solution of equation 1 (Sambridge and Mosengard, 2002). A Markov Chain Monte Carlo method is an algorithm that samples different points in the model space according to a random walk. In each step, the probability of transition to the following point depends only on the current sampled model. in this work among the many MCMC algorithms, we use the Metropolis-Hasting method (Hastings, 1970), which can be simply summarized in a two-step procedure: in the first step, a candidate model is drawn from the prior PDF, while in the second step this model is accepted with a probability that depends on its fits with the observed data. If the candidate model is accepted the random walk moves to such model, otherwise the current model is repeated in the walk, and another candidate model is drawn and its fit with the observed data is evaluated. The ensemble of accepted models is the final output of the algorithm that can be used to numerically compute the posterior PDF. Once that a candidate model is drawn from the prior probability, it is accepted following the so-called Metropolis rule. According to that, the probability of accepting a candidate model (usually called the acceptance ratio) is:

$$\alpha = \min\left[1, \frac{p(\mathbf{d} \mid \mathbf{k}_{\mathbf{cand}})}{p(\mathbf{d} \mid \mathbf{k}_{\mathbf{curr}})}\right] \quad (2)$$

where $\mathbf{k}_{\mathbf{cand}}$ is the candidate model and $\mathbf{k}_{\mathbf{curr}}$ is the current model (the last model accepted during the random walk). Equation 2 indicates that if the likelihood of the candidate model is higher than the likelihood of the current model, the candidate model is always accepted. Conversely, if the likelihood of the candidate models is lower than that of the current model, the candidate model is accepted with probability equal to $p(\mathbf{d}|\mathbf{k}_{\mathbf{cand}})/p(\mathbf{d}|\mathbf{k}_{\mathbf{curr}})$. It can be demonstrated that if the candidate models are generated according to the prior PDF, the Metropolis rule generates a random walk that samples the target posterior PDF (Mosegaard and Tarantola 1995). Generally, to increase the

reliability of the results, multiple random walks are sequentially performed starting from different parts in the model space, and the models collected by each walk are combined to derive the posterior PDF. In addition, it is known that the samples accepted at the beginning of the chain (during the so called “burn-in” period) may not accurately represent the posterior probability density function. For this reason, these models are usually not considered in the computation of the posterior PDF. Obviously, the length of the burn-in phase depends on the complexity of the problem being solved and on the recipe used to implement the MCMC algorithm. If needed, the potential scale reduction factor can be used to monitor the convergence of the MCMC algorithm to a stable posterior PDF (Gelman et al. 2013).

The two-step approach (TS)

The main objective of the two-step approach is to provide a fast and reliable inversion algorithm for seismic-reservoir characterization. This method estimates reservoir properties and litho-fluid facies from seismic data in two sequential steps. In the first step, a Bayesian linear inversion technique (valid for weak elastic contrasts and a small-range of reflection angles) is used to estimate the posterior probability $p(\mathbf{r}|\mathbf{d})$ of petrophysical properties conditioned upon the observed pre-stack data. To make the inversion computationally fast, we integrate the petrophysical and the elastic inversions into a single inversion step, in which the petrophysical properties are directly estimated from seismic data under the assumption of Gaussian distributed reservoir properties:

$$p(\mathbf{r}) = N(\mathbf{r}; \boldsymbol{\mu}_{\mathbf{r}}, \Sigma_{\mathbf{r}}) \quad (3)$$

where N indicate the Gaussian PDF, with mean vector and covariance matrix expressed by $\boldsymbol{\mu}_{\mathbf{r}}$ and $\Sigma_{\mathbf{r}}$, respectively**.** The statistical properties of this a-priori PDF can be easily derived from the analysis of available borehole logs.

Most of amplitude versus angle inversion algorithms adopt an elastic forward operator based on a time-continuous linear approximation of the Zoeppritz equations. For example, this forward

operator can be parameterized in terms of the *Vp*, *Vs* and density contrasts at the reflecting interface (Stolt and Weglein, 1985):

$$Rpp(t,\theta) = \alpha_{Vp}(t,\theta)\frac{\partial}{\partial t}\ln Vp + \alpha_{Vs}(t,\theta)\frac{\partial}{\partial t}\ln Vs + \alpha_{\rho}(t,\theta)\frac{\partial}{\partial t}\ln \rho \quad (4)$$

where *Rpp* is P-wave reflection coefficients, *t* is the time, θ is the incidence angle and $\alpha_{Vp}(\theta)$, $\alpha_{Vs}(\theta)$ and $\alpha_{\rho}(\theta)$ are given (for each time position) by:

$$\alpha_{Vp}(\theta) = \frac{1}{2}\left(1+\tan^2(\theta)\right) \quad (5.1)$$

$$\alpha_{Vs}(\theta) = -4\frac{\overline{Vs}^2}{\overline{Vp}^2}\sin^2(\theta) \quad (5.2)$$

$$\alpha_{\rho}(\theta) = \frac{1}{2}\left(1-4\frac{\overline{Vs}^2}{\overline{Vp}^2}\sin^2(\theta)\right) \quad (5.3)$$

where $\overline{Vp}$ and $\overline{Vs}$ are the averages of P-wave and S-wave velocities across the reflecting interface. In matrix notation equation 4 can be written as:

$$\mathbf{Rpp} = \mathbf{ADm} \quad (6)$$

where the derivative matrix **D** approximates the time derivatives of ln(*Vp*), ln(*Vs*) and ln(ρ), whereas the sparse matrix **A** contains discrete time samples of the coefficients $\alpha_{Vp}(\theta)$, $\alpha_{Vs}(\theta)$ and $\alpha_{\rho}(\theta)$. The equation that relates the elastic properties to the seismic data can be written as follows:

$$\mathbf{d} = \mathbf{WADm} = \mathbf{G_m m} \quad (7)$$

where $\mathbf{G_m}$ is the seismic-elastic forward operator (for brevity called elastic forward modelling from here on) that groups together the wavelet convolutional matrix **W,** the derivative matrix **D** and the matrix **A.** For a detailed description of the parameterization of **W** and **A** see Appendix B of Buland and Omre (2003). Being $\mathbf{G_m}$ a linear forward operator and by assuming a multivariate Gaussian a-priori PDF for **m** (that is a log-Gaussian PDF for *Vp, Vs* and density), the estimated elastic parameters **m,** are again represented by a multivariate Gaussian a posteriori PDF with analytical expressions for the mean and the covariance (Buland and Omre, 2003):

$$\boldsymbol{\mu}_{\mathbf{m|d}} = \boldsymbol{\mu}_{\mathbf{m}} + (\mathbf{G}_{\mathbf{m}}\boldsymbol{\Sigma}_{\mathbf{m}})^{T}(\boldsymbol{\Sigma}_{\mathbf{d}})^{-1}(\mathbf{d} - \mathbf{G}_{\mathbf{m}}\boldsymbol{\mu}_{\mathbf{m}}) \quad (8)$$

$$\boldsymbol{\Sigma}_{\mathbf{m|d}} = \boldsymbol{\Sigma}_{\mathbf{m}} - (\mathbf{G}_{\mathbf{m}}\boldsymbol{\Sigma}_{\mathbf{m}})^{T}(\boldsymbol{\Sigma}_{\mathbf{d}})^{-1}(\mathbf{G}_{\mathbf{m}}\boldsymbol{\Sigma}_{\mathbf{m}}) \quad (9)$$

where, $\mu_{\mathbf{m}}$ and $\Sigma_{\mathbf{m}}$ are the mean and the covariance of the a-priori PDF of **m,** while $\boldsymbol{\Sigma}_{\mathbf{d}} = \mathbf{G}_{\mathbf{m}}\boldsymbol{\Sigma}_{\mathbf{m}}\mathbf{G}_{\mathbf{m}}^{\mathbf{T}} + \boldsymbol{\Sigma}_{\mathbf{n}}$, where $\boldsymbol{\Sigma}_{\mathbf{n}}$ is the covariance matrix expressing the noise in the seismic data.

In order to implement the TS approach, the time-continuous reflectivity function of equation 4 is reparametrized in terms of petrophysical properties. To this aim a linear rock-physics model relating the petrophysical properties to the natural logarithm of the elastic attributes, can be defined as follows:

$$\ln(Vp) = a_1 + a_2 z + a_3\varphi + a_4 Sw + a_5 Sh; \quad (10.1)$$
$$\ln(Vs) = b_1 + b_2 z + b_3\varphi + b_4 Sw + b_5 Sh; \quad (10.2)$$
$$\ln(\rho) = c_1 + c_2 z + c_3\varphi + c_4 Sw + c_5 Sh; \quad (10.3)$$

where z is the depth, while a, b and c are the regression coefficients that can determined by a stepwise regression of well log or core information. Differentiating equations 10.1-3 sample-by-sample by applying the Δ operation, leads to:

$$\Delta\ln(Vp) = a_3\Delta\varphi + a_4\Delta Sw + a_5\Delta Sh; \quad (11.1)$$
$$\Delta\ln(Vs) = b_3\Delta\varphi + b_4\Delta Sw + b_5\Delta Sh; \quad (11.2)$$
$$\Delta\ln(\rho) = c_3\Delta\varphi + c_4\Delta Sw + c_5\Delta Sh; \quad (11.3)$$

in which the z term has been eliminated by assuming a negligible depth interval between adjacent samples. Equations 11.1-3 express the contrasts in elastic properties in terms of contrasts in petrophysical properties. Equations 11 can be compactly written in matrix notation as:

$$\mathbf{Dm} = \mathbf{BDr} \quad (12)$$

where **B** is a sparse matrix that contains the a, b and c coefficients of equations 11.1-3. By combining equation 6 and equation 12, gives:

$$\mathbf{Rpp} = \mathbf{ABDr} = \mathbf{FDr} \quad (13)$$

Writing equation 13 in a time continuous form, similar to that of equation 4, results in:

$$Rpp(t,\theta) = f_{\varphi}(t,\theta)\frac{\partial}{\partial t}\varphi + f_{Sw}(t,\theta)\frac{\partial}{\partial t}S_w + f_{Sh}(t,\theta)\frac{\partial}{\partial t}S_h \qquad (14)$$

where $f_{\varphi}(t,\theta)$, $f_{Sw}(t,\theta)$, and $f_{Sh}(t,\theta)$ are the discrete time samples contained in matrix **F** and expressing the influence of the petrophysical properties in the P-wave reflection coefficients. Now by adding the convolutional matrix **W** to equation 13 leads to:

$$\mathbf{d} = \mathbf{WABDr} = \mathbf{WFDr} = \mathbf{G_r r} \qquad (15)$$

where $\mathbf{G_r}$ is the seismic-petrophysical forward modelling (for brevity called petrophysical forward modelling from here on) that directly links the seismic response **d** to the petrophysical properties **r**. The forward modelling $\mathbf{G_r}$ is used to cast the petrophysical inversion into a Bayesian framework. Similarly to equations 8 and 9, the mean ($\mu_{\mathbf{r|d}}$) and variance ($\Sigma_{\mathbf{r|d}}$) of the posterior PDF of petrophysical properties conditioned upon the observed seismic data $p(\mathbf{r}|\mathbf{d})$ can be written as:

$$\boldsymbol{\mu}_{\mathbf{r|d}} = \boldsymbol{\mu}_{\mathbf{r}} + \boldsymbol{\Sigma}_{\mathbf{r}}\mathbf{G}_{\mathbf{r}}^{\mathbf{T}}(\mathbf{G}_{\mathbf{r}}\boldsymbol{\Sigma}_{\mathbf{r}}\mathbf{G}_{\mathbf{r}}^{\mathbf{T}} + \boldsymbol{\Sigma}_{\mathbf{e}})^{-1}(\mathbf{d} - \mathbf{G}_{\mathbf{r}}\boldsymbol{\mu}_{\mathbf{r}}); \qquad (16.1)$$

$$\boldsymbol{\Sigma}_{\mathbf{r|d}} = \boldsymbol{\Sigma}_{\mathbf{r}} - \boldsymbol{\Sigma}_{\mathbf{r}}\mathbf{G}_{\mathbf{r}}^{\mathbf{T}}(\mathbf{G}_{\mathbf{r}}\boldsymbol{\Sigma}_{\mathbf{r}}\mathbf{G}_{\mathbf{r}}^{\mathbf{T}} + \boldsymbol{\Sigma}_{\mathbf{e}})^{-1}\mathbf{G}_{\mathbf{r}}\boldsymbol{\Sigma}_{\mathbf{r}}; \qquad (16.2)$$

where $\boldsymbol{\Sigma}_{\mathbf{e}}$ is the matrix expressing the error term (see discussion below). The matrix $\boldsymbol{\Sigma}_{\mathbf{r}}$ expresses both the mutual correlation of petrophysical properties and their vertical variability. In particular, their mutual correlation is given by a stationary covariance matrix, while the vertical correlation is obtained by multiplying (Kronecker product) the stationary covariance matrix by a matrix expressing the vertical correlation. This vertical correlation is given by a second-order exponential function (Buland and Omre, 2003) that approximates the actual vertical variability of petrophysical properties:

$$\nu_t(\tau;\xi_1;\xi_2) = \frac{1}{2}\exp\left(-\left(\frac{\tau}{\xi_1}\right)^2\right) + \frac{1}{2}\left(1 - \frac{2\tau^2}{\xi_2^2}\right)\exp\left(-\left(\frac{\tau}{\xi_2}\right)^2\right) \qquad (17)$$

where τ is the time-lag and, ξ_1 and ξ_2 are the parameters characterizing the temporal dependency. Both the stationary covariance matrix of petrophysical properties and the vertical correlation function, can be determined from available well log information. In our approach $\boldsymbol{\Sigma}_{\mathbf{e}}$ includes both

the error affecting the seismic data $\boldsymbol{\Sigma_n}$, and the uncertainty related to the derived linear RPM ($\boldsymbol{\Sigma_{RPM}}$). The matrix $\boldsymbol{\Sigma_e}$ can be expressed as (Gouveia and Scales 1998; Aleardi et al. 2017a):

$$\sum_{\mathbf{e}} = \sum_{\mathbf{n}} + \sum_{\mathbf{RPM}} \qquad (18)$$

To compute the matrix $\boldsymbol{\Sigma_n}$ we assume a normally distributed random noise with a null mean value and a diagonal covariance matrix. More in detail, $\boldsymbol{\Sigma_n}$ is computed by comparing adjacent seismic gathers, and by assuming that they are produced by similar petrophysical properties. This implies that the differences between these gathers are only due to noise contamination. If the assumption that only random noise contaminates the observed data holds, this procedure gives a realistic estimation of the noise variance. If coherent noise (residuals of multiples, suboptimal normal-move-out corrections) contaminate the data, this approach will result in an overestimation of the random noise. More in detail, let $\mathbf{D_j}$ be the matrix containing along each column, the *j*-th seismic gather $\mathbf{d_j}$ and the *q* adjacent gathers:

$$\mathbf{D_j} = (\mathbf{d_{j-q/2}}, \ldots, \mathbf{d_j}, \ldots, \mathbf{d_{j+q/2}}) \qquad (19)$$

Then, the matrix $\boldsymbol{\Sigma^j_n}$ that represents the noise that affects the *j*-th seismic gather is computed as:

$$\sum\nolimits_{\mathbf{n}}^{\mathbf{j}} = \mathbf{I} \cdot \mathrm{cov}(\mathbf{D_j}) \qquad (20)$$

where $\mathbf{I}$ is the identity matrix.

The differences between the logged elastic properties and the elastic properties predicted by the linear RPM, are used to derive the $\boldsymbol{\Sigma}_{\mathrm{RPM}}$ matrix. We assume that this difference follows a Gaussian PDF with a given covariance matrix and a null mean value:

$$p_{TS}(\boldsymbol{\varepsilon}) = N(\boldsymbol{\varepsilon}; \boldsymbol{\mu}_{\boldsymbol{\varepsilon}} = 0, \boldsymbol{\Sigma}_{\boldsymbol{\varepsilon}}) \qquad (21)$$

Obviously, a similar approach can be used to define the uncertainties affecting the theoretical RPM used in the SL approach ($p_{SL}(\boldsymbol{\varepsilon})$).

After defining the $p_{TS}(\boldsymbol{\varepsilon})$, we use the following Monte Carlo approach to derive the $\boldsymbol{\Sigma}_{\mathrm{RPM}}$ matrix:

1. Consider a 1D vertical profile and draw random values from the a-priori PDF of petrophysical properties $p(\mathbf{r})$, taking into account both their mutual and their vertical correlation;
2. Apply the empirical RPM to convert the petrophysical properties into the elastic properties;
3. Perturb the elastic properties by adding random vector drawn from $p_{TS}(\boldsymbol{\varepsilon})$. Also in this case, the vertical correlation is considered;
4. Use equation 7 to derive the seismic data;
5. Repeat steps 3 and 4 q-times and collect all the q seismic gathers, each one generated by a perturbation of the elastic properties according to the $p_{TS}(\boldsymbol{\varepsilon})$ PDF;
6. Let $\mathbf{D^s_q}$ be the matrix containing the q-th simulated seismic data ($\mathbf{d^s}$) along each column:

$$\mathbf{D^s_q} = (\mathbf{d^s_1}, \mathbf{d^s_2}, ..., \mathbf{d^s_q}) \qquad (22)$$

then the $\boldsymbol{\Sigma}_{\mathrm{RPM}}$ matrix is computed as follows:

$$\Sigma_{\mathbf{RPM}} = \mathrm{cov}(\mathbf{D^s_q}) \qquad (23)$$

In other words, the differences between the q simulated seismic gathers quantify the fluctuations in the seismic response related to uncertainties in the rock-physics model. To prevent overfitting the data, additional sources of errors can be added to equation 18, such as uncertainties in the estimated source wavelet, modelling errors, or else uncertainties related to the different scale of well log data (used to derive the RPM) and seismic data (the input of the inversion). To this end, Aleardi et al. (2017b) adopted an approach based on Backus averaging and Monte Carlo simulations. However, in this work only the error in the seismic data and the uncertainties in the rock-physics model are accounted for in the inversion.

The second step of the TS algorithm is the litho-fluid facies classification, in which the outcomes of the petrophysical inversion, namely the $p(\mathbf{r}|\mathbf{d})$ PDF, are combined with a downward Markov-

chain prior model (as in Larsen et al., 2006) in order to derive the posterior PDF of litho-fluid facies conditioned upon the observed data:

$$p(\mathbf{f}_t \mid d_t) = \prod_t \prod p(\mathbf{f}_t \mid \mathbf{f}_{t-1}) \int p(\mathbf{r}_t \mid \mathbf{f}_t)\, p(\mathbf{r}_t \mid \mathbf{d}) \mathbf{dr} \qquad (24)$$

where t indicates the time position, while the probability $p(\mathbf{f_t}|\mathbf{f_{t-1}})$ can be obtained from the downward Markov-chain transition matrix $\mathbf{T_m}$ of litho-fluid classes. In the transition matrix, each element a_{ij} along the i-th row and j-th column expresses the probability of a transition from the facies i located above the interface to the facies j located below. In the following application, we consider three facies: shale, brine sand and gas sand that are defined on previous geological knowledge about the investigated area and on the basis of well log data investigating the target zone. The **T** matrix derived from well log information is the following:

$$\mathbf{T} = \begin{bmatrix} 0.909 & 0.056 & 0.035 \\ 0.120 & 0.880 & 0 \\ 0.056 & 0.037 & 0.907 \end{bmatrix} \qquad (25)$$

From top to bottom, rows correspond to shale, brine sand, and gas sand at generic vertical position t, while from left to right the columns refer to shale, brine sand, and gas sand at vertical position t-1, respectively. Note that we impose a null probability for the downward transition from brine sand to gas sand.

The single-loop inversion algorithm (SL)

The single-loop approach was implemented to verify the reliability of the predictions given by the TS method. In particular, the comparison between the results provided by the TS and SL algorithms, allows us to assess the suitability of the linear RPM, of the Gaussian a-priori model, and of the weak contrasts assumption, for the investigated reservoir. For this reason, the SL algorithm uses a non-linear theoretical RPM, considers the exact Zoepprtiz equations as forward modelling, and more realistically assumes a Gaussian mixture (GM) a-priori PDF for the petrophysical properties (Grana and Della Rossa, 2010). The GM assumption implies that the petrophysical

properties are Gaussian distributed within each facies. In the following application, we assume that the number of components of the GM-PDF corresponds to the number of facies considered (shale, brine sand, and gas sand). Mathematically, this probability density function can be written as:

$$p(\mathbf{r}) = \sum_{h=1}^{Q} \lambda_h \, p^h_{Sw,\varphi,Sh}(Sw,\varphi,Sh) = \sum_{h=1}^{Q} \lambda_h \, N(Sw,\varphi,Sh;\boldsymbol{\mu}^h_{Sw,\varphi,Sh},\Sigma^h_{Sw,\varphi,Sh}) = \sum_{h=1}^{Q} \lambda_h \, N(\mathbf{r};\boldsymbol{\mu}^h_{\mathbf{r}},\Sigma^h_{\mathbf{r}}) \quad (26)$$

where Q is the total number of facies, λ_h represents the weights of the components (i.e., the proportion of the different facies), whereas $\boldsymbol{\mu}^h_{\mathbf{r}}$ and $\boldsymbol{\Sigma}^h_{\mathbf{r}}$ are the mean vector and the covariance matrix for each facies. The parameters that define the a-priori GM-PDF can be obtained applying the expectation maximization algorithm (Hastie et al. 2002) to the ensemble of available well log data.

Following the chain rule, the posterior PDF that is the target of the SL inversion algorithm, can be compactly written as follows:

$$p(\mathbf{e,r,f} \mid \mathbf{d}) = \frac{p(\mathbf{d} \mid \mathbf{e,r,f})\, p(\mathbf{e} \mid \mathbf{r,f})\, p(\mathbf{r} \mid \mathbf{f})\, p(\mathbf{f})}{p(\mathbf{d})} \quad (27)$$

Note that in equation 27 the model vector **k** of equation 1 now contains an ensemble of litho-fluid facies, petrophysical properties and elastic properties **k**=[**f,r,e**]. In the implemented SL algorithm, the following steps are used to define the initial model at the beginning of the chain:

1a) Define a vertical succession of litho-fluid facies according to the derived downward transition matrix (equation 25);

2a) Define the petrophysical parameters by drawing random numbers from the conditional probability $p(\mathbf{r}|\mathbf{f})$. In our case, in which a GM-PDF is assumed for the petrophysical properties, this step reduces to draw random candidates from the prior probability $N(\mathbf{r};\boldsymbol{\mu}^h_{\mathbf{r}},\Sigma^h_{\mathbf{r}})$. The mutual correlation of petrophysical properties is modelled by a stationary covariance matrix, while a vertical correlation function based on equation 17 is used to model the vertical correlation;

3a) Apply the rock-physics model (in our case a theoretical, non-linear, RPM) to convert the petrophysical properties into the elastic parameters (*Vp*, *Vs* and density);

4a) Add to the derived elastic parameters the uncertainties associated to the rock physics model expressed by $p_{SL}(\boldsymbol{\varepsilon})$. Also in this case, we consider the vertical correlation when drawing random numbers from $p_{SL}(\boldsymbol{\varepsilon})$. Step 3a) and 4a) are used to pick the elastic parameters from the conditional probability $p(\mathbf{e}|\mathbf{r},\mathbf{f})$;

5a) Compute the likelihood for the considered model $p(\mathbf{d}|\mathbf{m},\mathbf{r},\mathbf{f})$. The seismic response associated to this model is computed by using a convolutional forward modelling based on the exact Zoeppritz equations. The so derived seismic data is compared with the observed data, in order to compute the likelihood value. The likelihood function we consider is based on a least-squares measure of misfit in which the noise is assumed to be normally distributed with a null mean value and a diagonal covariance matrix $\boldsymbol{\Sigma}_{\mathbf{n}}$. Under this assumption, the likelihood value is:

$$p(\mathbf{d}\,|\,\mathbf{e},\mathbf{r},\mathbf{f}) = \frac{1}{((2\pi)^{w}\,|\,\Sigma_{\mathbf{n}}\,|)^{1/2}} \exp\left(-\frac{1}{2}\mathbf{v}^{T}\,\Sigma_{\mathbf{n}}^{-1}\,\mathbf{v}\right) \qquad (28)$$

in which w is the number of data points and $\mathbf{v}$ is the data misfit vector. The matrix $\boldsymbol{\Sigma}_{\mathbf{n}}$ can be computed with an approach similar to that previously described (equations 19 and 20)

6a) Accept the initial model as the current model.

After generating the initial model, a candidate model must be defined. The steps advocated to this aim are the following:

1b) Select q time positions along the vertical profile by drawing q integer random numbers uniformly distributed, each one representing a given time sample along the considered time interval;

2b) For each q-th time position, draw a random number γ uniformly distributed over [0,1];

3b) If γ <0.3, take the current model and perturb the litho-fluid facies in the considered q-th position. This step reduces to draw a random candidate from the prior PDF $p(\mathbf{f})$ that represents the actual proportion of litho-fluid facies derived from matrix $\mathbf{T}$. For a given time position q, the facies perturbation is accepted if a random number α uniformly distributed over [0,1] satisfies:

$$\mathbf{T}(i,\,j) \geq \alpha \qquad (29)$$

where *i* identify the facies at the time position *q*-1 and *j* is the proposed facies at position *q*. If the perturbation is accepted, draw a random sample from $p(\mathbf{r}|\mathbf{f})$ to define the petrophysical properties of the candidate model at the position *q*. In order to maintain vertically correlated petrophysical properties, we propagate the local perturbation at the *q*-th time position along the entire vertical profile. In particular, for a perturbed time position *q*, we compute the difference between the current model and the candidate, perturbed, model in that position:

$$\mathbf{r}_{\mathbf{diff}}^{\mathbf{q}} = \mathbf{r}_{\mathbf{cand}}^{\mathbf{q}} - \mathbf{r}_{\mathbf{curr}}^{\mathbf{q}} \qquad (30)$$

This difference is then convolved with a delta Dirac function located at the *q*-th time position (t_q):

$$\boldsymbol{\delta}_{\mathbf{r}}(\mathbf{t}-\mathbf{t}_{\mathbf{q}}) = \mathbf{r}_{\mathbf{diff}}^{\mathbf{q}} \otimes \boldsymbol{\delta}(\mathbf{t}-\mathbf{t}_{\mathbf{q}}) \qquad (31)$$

Then the total perturbation vector $\mathbf{r_{pert}}$ is derived by convolving $\boldsymbol{\delta}(\mathbf{t}-\mathbf{t_q})$ with the vertical correlation function $\mathbf{v(t)}$:

$$\mathbf{r}_{\mathbf{pert}} = \boldsymbol{\delta}_{\mathbf{r}}(\mathbf{t}-\mathbf{t}_{\mathbf{q}}) \otimes \mathbf{v(t)} \qquad (32)$$

Finally, the candidate, perturbed, petrophysical model is computed as follows:

$$\mathbf{r}_{\mathbf{cand}} = \mathbf{r}_{\mathbf{curr}} + \mathbf{r}_{\mathbf{pert}} \qquad (33)$$

4b) If $\gamma \geq 0.3$, define the petrophysical properties of the candidate model by perturbing the petrophysical properties of the current model in the *q*-th time position. This perturbation follows a random walk that samples the $p(\mathbf{r}|\mathbf{f})$. The litho-fluid facies in this case are kept fixed. Being the prior PDF of the petrophysical properties a GM, this perturbation follows a random walk that samples the normal prior density function $N(\mathbf{r};\boldsymbol{\mu}_{\mathbf{r}}^{h},\sum_{\mathbf{r}}^{h})$. To get a better understanding of this step, let us consider a continuous variable *x* and a target probability $p(x)$; the algorithm will generate a candidate value x_p by perturbing *x*:

$$x_p = x + \Delta x \qquad (34)$$

where the PDF of the perturbation Δx has null mean value and a variance that must be small compared to the variance of $p(x)$ and that should be set in order to accept a reasonable fraction of

candidate models. Indeed, as discussed in Agostinetti and Malinverno (2010) the method used to perturb the current model assumes particular importance in a MCMC inversion. A too weak perturbation is computationally expensive and the convergence of the algorithm will be very slow. Conversely, a too strong perturbation is inefficient because tends to generate proposed models with a likelihood values usually lower than that of the current model. There is not a unique rule to set the amplitude of the perturbation; however, experience has shown that an acceptance ratio (the ratio between the number of accepted models and the number of proposed models) between 0.2-0.5 is optimal in most applications (Mosegaard 2006). In the implemented MCMC algorithm we follow this general rule in setting the parameters that define the model perturbations, the number of time positions to be perturbed at each iteration, and the other user-defined parameters of the MCMC algorithm. After perturbing x, the algorithm moves to x_p with a probability:

$$\alpha = \min\left[1, \frac{p(x_p)}{p(x)}\right] \qquad (35)$$

If a Gaussian probability is assumed, the ratio $p(x_p)/p(x)$ reduces to:

$$\frac{p(x_p)}{p(x)} = \exp\left(-\frac{(x-\mu_x)^2 - (x_p-\mu_x)^2}{2\sigma_x{}^2}\right) \qquad (36)$$

In our application μ_x and σ_x are the mean and the standard deviation of the normal PDF $N(\mathbf{r};\boldsymbol{\mu}_{\mathbf{r}}^h,\sum_{\mathbf{r}}^h)$. Similarly to step 3b), the local perturbation at the q-th time position is propagated along the vertical profile of petrophysical properties with the method previously described;

5b) Repeat 2b, 3b or 4b for each q-th time position.

After step 5b) we compute the elastic parameters associated to the candidate model and its likelihood value by repeating steps 3a), 4a) and 5a). Finally, the candidate model is accepted according to the Metropolis rule. If the candidate model is accepted $\mathbf{k}_{\text{curr}}=\mathbf{k}_{\text{cand}}$, and if the burn-in period is over k_{cand} is collected. Then, the steps 1b-4b are repeated until the desired number of accepted model is reached. This procedure draws models from $p(\mathbf{f})$, $p(\mathbf{r}|\mathbf{f})$, $p(\mathbf{e}|\mathbf{r},\mathbf{f})$ and $p(\mathbf{d}|\mathbf{e},\mathbf{r},\mathbf{f})$ and the posterior PDF $p(\mathbf{r},\mathbf{e},\mathbf{f}|\mathrm{d})$ can be numerically compute from the collected ensemble of

models. In all inversion tests described in the following, we use 15 different random walks that start from different initial models. In each walk 7000 models are collected and only the last 3500 are considered in the computation of the final PDF, thus considering a burn-in period of 3500 models.

Deriving and validating the linear rock-physics model

The reservoir considered in this work is located in a shale-sand sequence and is constituted by gas-bearing sands at the depth range of 900–1000 m. Borehole logs from 7 wells provide elastic and petrophysical information needed to fully characterize the reservoir rocks in terms of *Vp*, *Vs*, density, effective porosity, water-saturation and shaliness (i.e. dry clay + clay-bound water). The reservoir sand is rather clean with no cementation and low clay content; effective porosity ranges from 0 to 35%, while gas saturation usually varies between 0% and 80%. With the aim to derive a comprehensive RPM, valid both for reservoir sands and for the intra-reservoir shales, theoretical models, and linear and non-linear regression approaches have been tested. In particular, here we limit our attention to two RPMs:

$$[\ln(Vp), \ln(Vs), \ln(\rho)] = f^{1}_{RPM}(z, Sw, \varphi, Sh) \qquad (37.1)$$

$$[Vp, Vs, \rho] = f^{2}_{RPM}(z, Sw, \varphi, Sh) \qquad (37.2)$$

the f^{1}_{RPM} is an empirical, linear RPM applied in the TS approach, whereas f^{2}_{RPM} is a theoretical, non-linear, RPM based on granular media models (Hertz-Mindlin contact theory, Hashin-Shtrikman bound and Gassmann model) used by the SL algorithm. In particular, this section is aimed at demonstrating that a linear RPM is suitable for reservoir characterization in the investigated area. The linear RPM has been estimated using a stepwise regression approach performed over a set of more than 4000 well log samples for *Vp* and density and more than 2000 sample for *Vs*. The f^{1}_{RPM} is expressed by the following relations:

$$\ln(Vp) = 7.6906 + 4.4332\times10^{-6} z - 0.0101\varphi + 0.0011Sw - 0.0021Sh \qquad (38.1)$$

$$\ln(Vs) = 7.3684 + 6.7678\times10^{-5} z - 0.0184\varphi + 2.6807\times10^{-4} Sw - 0.0061Sh \qquad (38.2)$$

$$\ln(\rho) = 7.7268 + 1.89\times10^{-5} z - 0.0060\varphi + 0.0010Sw - 0.0016Sh \qquad (38.3)$$

where *Vp* and *Vs* are expressed in *m/s*, density in kg/m^3, *z* in *m*, and the petrophysical properties in percentage. As a first rough appraisal of the empirical RPM, note that the estimated equations show a physically-consistent behavior. In particular, the depth shows a very limited influence on the elastic properties due to the limited depth range (centered around the target interval), that has been considered in deriving the RPM. In addition, as expected, the *Vp*, *Vs* and density decrease with the increase of porosity. The increase of water saturation slightly increases the three elastic property values, while an increase of shaliness determines a decrease of seismic velocities and density. By observing the magnitude of the coefficient of equations 38.1-3 we conclude that the porosity is the parameter that plays the major role in controlling the elastic properties, followed by the shaliness and the water saturation. From these considerations, we expect that the porosity will be the best resolvable parameters in the inversion, while the shaliness and particularly the water saturations will be less resolvable. Figure 1 shows a comparison between logged elastic properties and the predictions given by the linear and the theoretical RPMs. The good match between the actual and the predicted properties evidences the reliability of both RPMs, and proves that in the investigated area, a linear RPM can reliability express the relation linking the elastic attributes to the petrophysical properties.

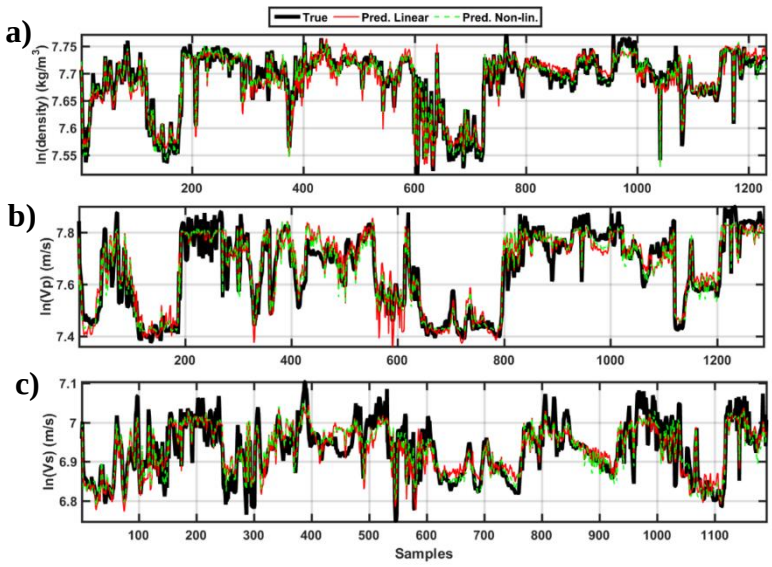

Figure 1: Comparison between logged elastic properties (black curves) and predicted properties by the empirical RPM (red curves) and by the theoretical RPM (green dashed curves). a), b) And c) refer to ln(density), ln(Vp) and ln(Vs), respectively. Note the very similar predictions given by the empirical and the theoretical RPMs. For the empirical RPM the resulting correlation coefficients are 0.94, 0.91 and 0.81 for density, Vp, and Vs respectively. For the theoretical RPM the resulting correlation coefficients are 0.94, 0.93 and 0.82 for density, Vp, and Vs respectively.

In Figure 2 are represented the so-called rock physics templates (RPTs) (Avseth et al. 2005) for the linear RPM, which are cross-plots showing the influence of the petrophysical properties on the elastic attributes (i.e. P-impedance, *Ip* and S-impedance, *Is*). Figure 2a shows the RPT derived from the actual well-log data and the associated petrophysical properties. We observe a decrease of *Ip* and *Is* as the water saturation, shaliness and as the porosity increase. These general trends are well matched by the RPTs derived from the empirical f^{1}_{RPM}, thus indicating the suitability of this RPM for reservoir characterization in the investigated zone.

The PDF of the error associated with the two RPMs can be derived by computing the difference between the logged elastic property values and the corresponding values predicted by each RPM. For the empirical RPM, we represent in Figure 3 the sample-by-sample difference between actual

and predicted P- and S-wave impedances (*Ip* and *Is*, respectively). By assuming that this difference is Gaussian distributed, we can compute the mean and the covariance of the error PDF associated to the empirical RPM ($p_{TS}(\boldsymbol{\varepsilon})$), which will be used to propagate the uncertainties in the RPM into the estimated petrophysical properties. In Figure 3 note that the derived $p_{TS}(\boldsymbol{\varepsilon})$ has a mean value very close to the assumed value of zero.

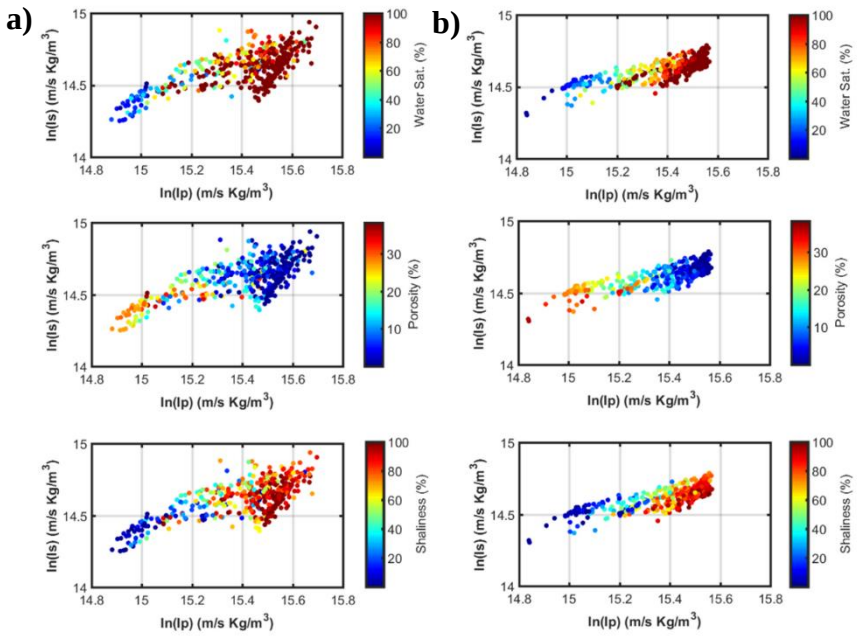

Figure 2: Comparison between actual and predicted RPTs by the empirical RPM of equation 38.1-3. a) RPTs derived from actual well log data and showing the influence of each petrophysical parameter on the natural logarithm of the P-impedance (Ip) and S-impedance (Is) values. The influence of water saturation, porosity and shaliness is represented from top to bottom. b) RPTs predicted by the empirical RPM. Note that the main trends visible in a) are well predicted by the estimated RPM.

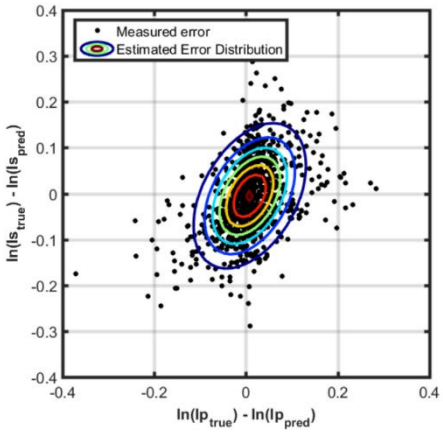

Figure 3: The error PDF $p_{TS}(\boldsymbol{\varepsilon})$ for the empirical RPM (f^{1}_{RPM}) that expresses the variability of elastic properties that is not described by the estimated rock-physics model. The black dots show the difference between the natural logarithm of actual and predicted Ip and Is values, whereas the colored contours represent the Gaussian PDF derived on the ensemble of black dots (blue and red colors code low and high probabilities, respectively).

As previously introduced, the geological knowledge on the investigated has been exploited to define the number of litho-fluid facies to be considered: shale, brine sand and gas sand. Figure 4 shows cross-plots of the natural logarithm of the logged *Vp, Vs* and density values within each considered facies around the reservoir zone. Note that the *Vp* progressively decreases passing from shale, to brine sand and to gas sand. The lower *Vp* value for the gas sand with respect to the brine sand, is related to the decrease in bulk modulus that occurs when gas replaces brine in the pore space. The density is characterized by a slight decrease when passing from shale to brine sand and a significant decrease when moving from brine sand to gas sand. This trend is associable to the lower density value that characterizes the gas with respect to brine. It is noteworthy that the *Vs* maintains an almost constant value across the three facies. This is probably related both to the depth interval where the reservoir is located, in which shale and sand are characterized by a similar *Vs* value, and also to the insensibility of the shear modulus to the saturating fluid.

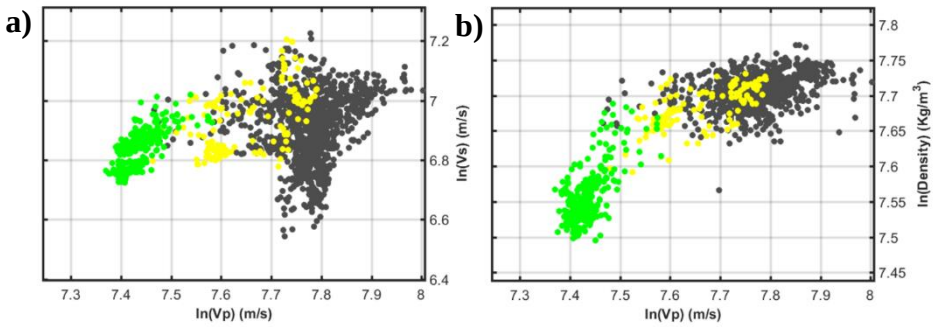

Figure 4: a) and b) Cross-plots showing the distribution of the natural logarithm of P-wave, S-wave velocities and density within each facies. The data have been extracted from the available well log data around the reservoir interval. Gray, yellow and green colors refer to shale, brine sand and gas sand, respectively. Note the decreases of density and Vp when moving from shale, to brine sand, and to gas sand and also the very similar S-wave velocity values within the three litho-fluid facies.

We now investigate if the different facies in the target area are characterized by peculiar and discernible AVA responses. Basing on the distribution of elastic properties of Figure 4 and by making use of a Monte Carlo simulation, we derive the expected PDFs of AVA responses in the target area for three different case: shale-shale, shale-brine sand and shale-gas sand interfaces. The procedure we use can be schematized in the following steps:

1) Consider a single reflecting interface separating the overlying shale and an underlying facies (shale, brine sand or gas sand);
2) Pick the elastic properties of the underlying and overlying layers from the associated PDFs that can be derived from the cross-plot of Figure 4;
3) Use the elastic properties resulting from 2) and equation 4 to compute the AVA response associated to the reflecting interface;
4) Store the resulting AVA response and iterate from 2) to 4) (in the following simulation we repeat this procedure 1500 times, that is until a stable PDF is attained).

From the ensemble of derived AVA responses, the corresponding PDF can be derived via a numerical approach (Avseth et al. 2005). From Figure 5 we observe that the shale-shale reflecting interface has, as expected, a reflection coefficient at normal incidence close to zero and negligible variations of the reflected amplitudes with the increase of the incidence angle. The shale-brine sand contact is associated with a slightly negative reflection coefficient at normal incidence that again tends to remain constant as the incidence angle increases. Finally, the shale-gas sand interface produces a negative reflection coefficient at normal incidence that remains almost constant when varying the incidence angle. Note that the slight *Vs* contrast between shale and sand determines negligible variations of the reflection coefficient as the incidence angle increases. If we consider the two-term Shuey approximation of the Zoeppritz equations, we can also derive the 2D PDF for the intercept and gradient values that characterize the expected AVA responses (Figure 6). This 2D representation allows us to better analyze the expected, theoretical, overlapping between the AVA responses associated to the different facies. Taking into consideration the Castagna and Swan (1997) classification, the shale-brine sand interface is mostly associated with a class II AVA response that is characterized by small intercept and gradient values. In the investigated case, the shale-gas sand interface does not generate a clear class III anomaly due to the weak *Vs* contrast between shale and sand.

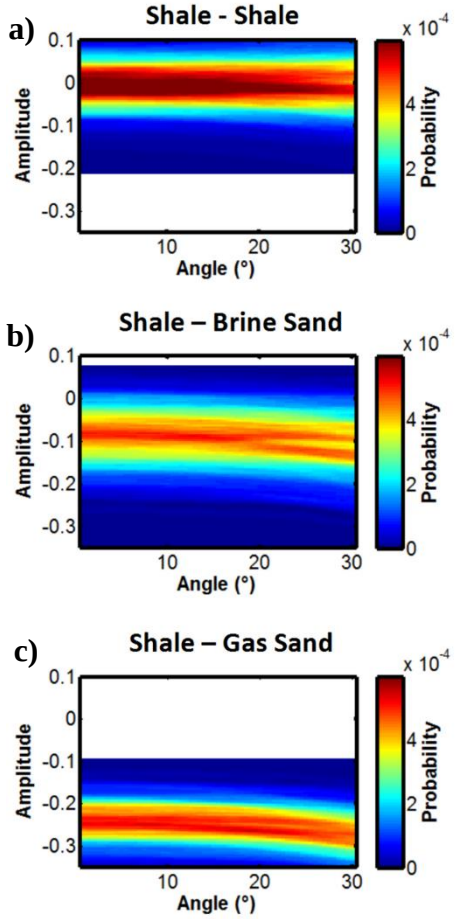

Figure 5: The expected PDFs of AVA responses in the target zone computed for a shale-shale contact (a), a shale-brine sand contact (b), and a shale-gas sand contact (c). In all cases note the limited variations of the reflected amplitudes as the incidence angle increases.

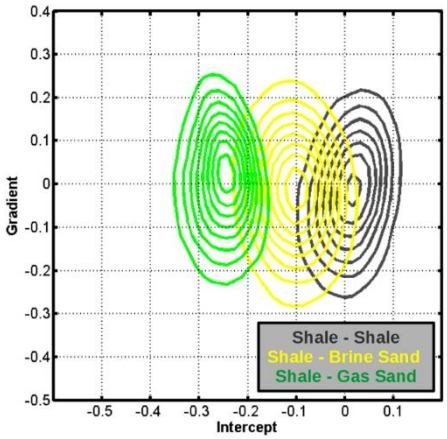

Figure 6: The expected PDF of the intercept and gradient values for the shale-shale, shale-brine sand and shale-gas sand reflecting interfaces.

Before describing the inversion results, we want to demonstrate the reliability of the derived linear RPM. To this end, we consider the borehole data pertaining to an exploration well (named well A in the following) and we compare the seismic data obtained from well A when using the elastic forward modelling of equation 7 and the petrophysical forward modelling of equation 15 (Figure 7). The close match between the seismic data resulting from the two forward modelling parameterizations is a first confirmation of the reliability of the derived RPM.

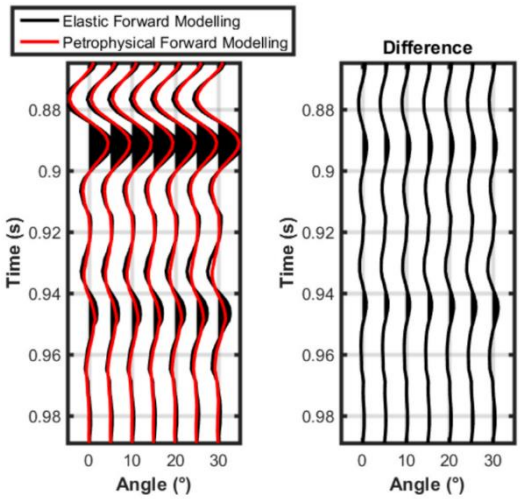

Figure 7: Comparison between synthetic CMP gathers obtained from well A by using an elastic forward modelling (equation 7) and a petrophysical forward modelling (equation 15) that was derived by incorporating the empirical RPM of equation 38.1-3 in the time-continuous approximation of the P-wave reflection coefficients. The negligible differences between the seismic data obtained by the two different forward modelling parameterizations, demonstrate the reliability of the derived linear RPM. For a better comparison, all the seismograms are represented with the same amplitude normalization.

Another more quantitative confirmation of the reliability of the empirical RPM of equation 38.1-3 can be obtained by directly inverting the logged *Vp*, *Vs* and density values for deriving the petrophysical properties. The mathematical framework of this inversion procedure is similar to that described in equation 15, in which the data vector **d** is now replaced by the vector of elastic properties **m**. The final results shown in Figure 8, demonstrate that the estimated maximum a

posterior (MAP) solution closely follows the actual petrophysical properties along the entire time interval we consider. As expected, we observe a high resolution for the porosity and lower resolutions for the shaliness and water saturation estimates. As previously discussed this fact is related to the different influences played by the petrophysical parameters in determining the elastic properties.

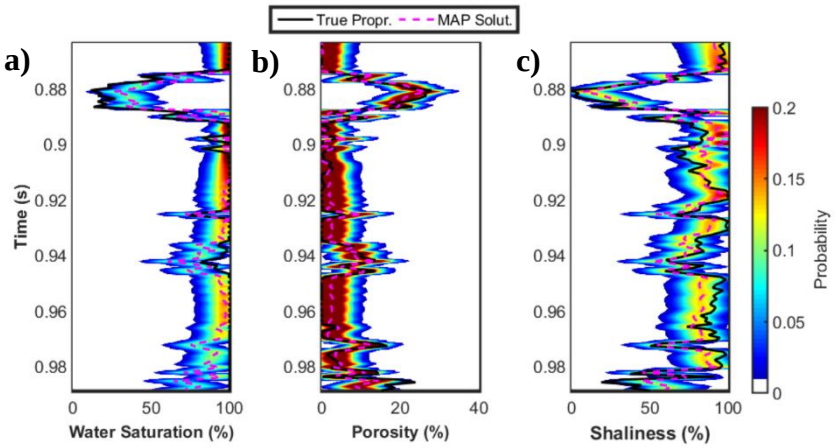

Figure 8: a), b) and c) Posterior PDFs for water saturation, porosity and shaliness estimated by the TS method when the logged elastic properties of Vp, Vs and density of well A are inverted. The match between the true properties values (continuous black lines) and the MAP solutions (dashed magenta lines) confirms the reliability of the empirical RPM of equation 38.1-3 and its suitability for reservoir characterization in the investigated area. Note the increase of uncertainties when passing from porosity, to shaliness and to water saturation.

Inversion of synthetic data

In the following, we describe the applications of the two implemented algorithms for the inversion of a synthetic seismic CMP gather that has been computed from actual well log measurements pertaining to well A. The seismic data have been computed with a convolutional forward modelling and using a 50 Hz Ricker wavelet that mimics the expected resolution of the available field seismic data.

Inversion with the TS algorithm

Figure 9 shows the results obtained by inverting the synthetic CMP associated to the considered well, within an angle range between 0 and 30 degrees. Note that the inversion has been able to predict, although with a low vertical resolution, the true petrophysical properties values. Again note that the expected resolution decreases moving from porosity, to shaliness and to water saturation.

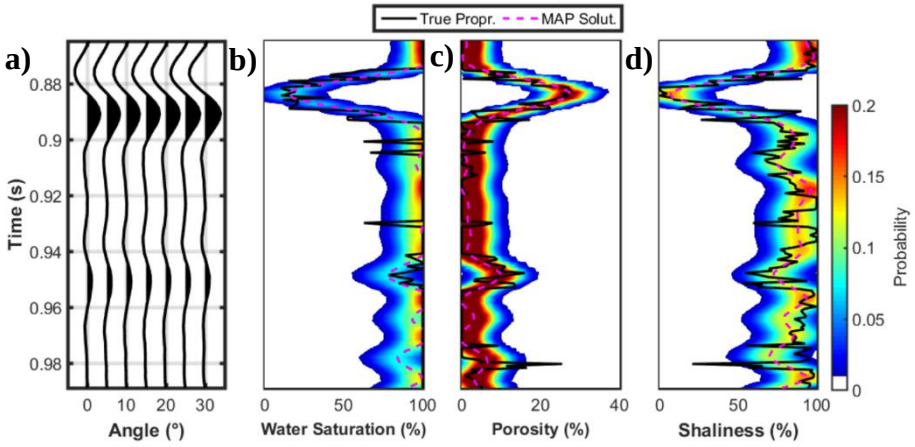

Figure 9: Inversion results provided by the TS algorithms for a synthetic CMP gather pertaining to well A. a), b) c) And d) represent the observed CMP gather, and the posterior PDFs for the petrophysical properties of water saturation, porosity and shaliness, respectively. The continuous black and dashed magenta lines display the logged property values and the MAP solution, respectively. Note that, although with a lower vertical resolution, the MAP solutions closely match the actual property values.

Figure 10 displays the results of litho-facies classification obtained from the outcomes of the petrophysical inversion shown in Figure 9. Note that the predicted facies profile closely matches the actual one derived from borehole information, although the filter effect introduced by the seismic wavelet impedes the identification of the thinnest layers, as the very thin brine saturated sand layer located at 0.982.

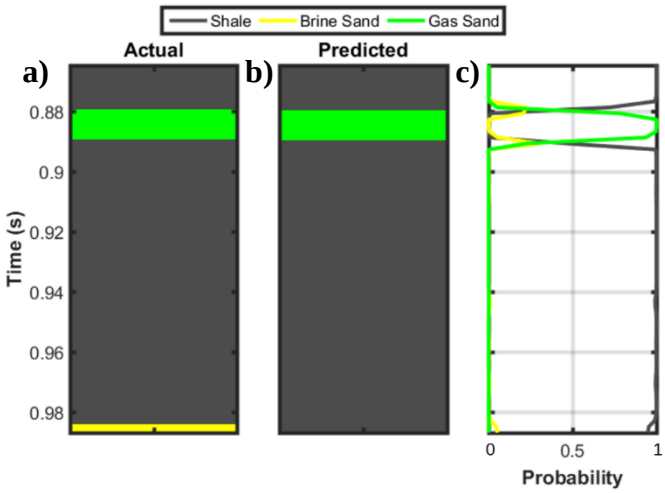

Figure 10: a) Actual facies profile at well A. b) And c) MAP solution and posterior PDF of litho-fluid facies provided by the TS algorithm for the synthetic inversion of the seismic data derived from well A, respectively. Note the close match between the actual and the predicted profiles.

Inversion with the SL algorithm

Before the seismic data inversion, we run the SL algorithm by setting the likelihood to unity in order to verify whether the proposed candidate models are distributed according to the prior probability density functions $p(\mathbf{f})$ and $p(\mathbf{r})$. Indeed, from equation 1 emerges that if the likelihood is fixed to one, the posterior PDF coincides with the prior PDF. Figure 11 shows the results of this exercise and demonstrates that the posterior PDF of litho-fluid facies and of petrophysical properties (water saturation, porosity and shaliness) are equal to the corresponding prior PDFs. This confirms the efficiency and the reliability of the implemented MCMC algorithm.

Figure 12 displays the posterior PDF $p(\mathbf{r}|\mathbf{d})$ obtained by inverting the synthetic seismic data pertaining to well A. Note that with respect to the inversion with the TS algorithm, the forward modelling engine of the SL approach based on the exact Zoeppritz equations, allow us to extend the angle range considered in the inversion (in the following test 0-40 degrees). Similarly, to the TS algorithm, also the SL approach has been able to predict the true petrophysical properties values. Note that the multimodal a priori PDF we consider for the petrophysical property tend to generate a multimodal posterior $p(\mathbf{r}|\mathbf{d})$. Figure 13 demonstrate that also the MAP solution for litho-fluid facies

and the probability $p(\mathbf{f}|\mathbf{d})$ are in accordance with the actual vertical facies profiles. Figure 14 shows an example of the first 1000 realizations (that are the accepted models) of the SL algorithm in the inversion of the synthetic seismic. Note that the model realizations of petrophysical properties and litho-fluid facies rapidly converge toward the actual well log information.

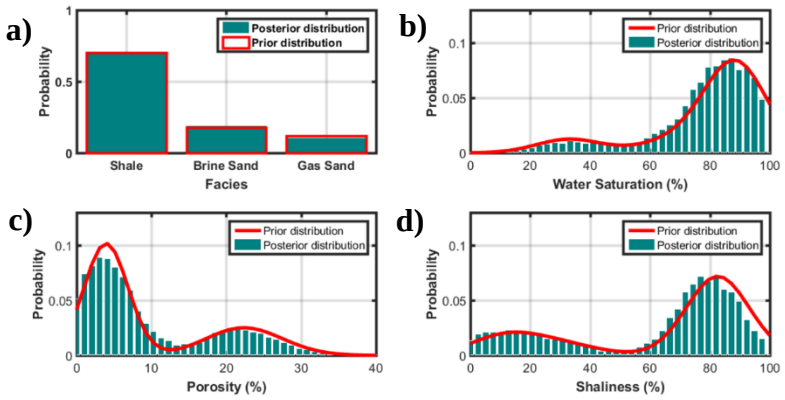

Figure 11: Comparison of prior and posterior PDFs of litho-fluid facies and petrophysical properties, derived by imposing in the SL inversion a likelihood value equal to one. a), b), c) And d) represent the PDFs of litho-fluid facies, water saturation, porosity and shaliness, respectively. The close match between prior and posterior PDFs proves that the distribution of the proposed models exactly follows the prior PDF.

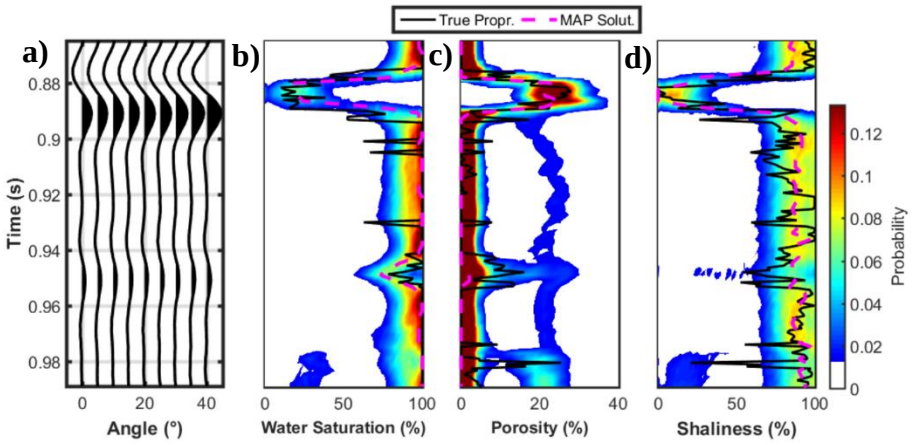

Figure 12: Inversion results provided by the SL algorithms for the synthetic CMP gather pertaining to well A. a), b) c) And d) represent the observed CMP gather, and the posterior PDFs for the petrophysical properties of water saturation, porosity and shaliness, respectively. The

continuous black and dashed magenta lines display the logged property values and the MAP solution, respectively. Note that, although with a lower vertical resolution, the MAP solutions closely match the true property values.

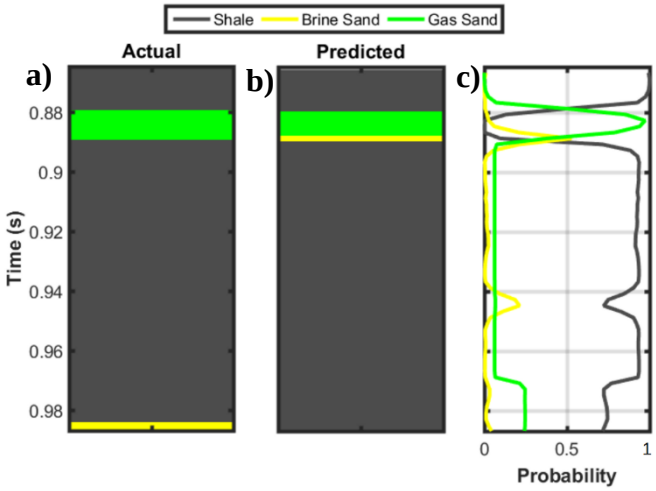

Figure 13: a) Actual facies profile at well A. b) and c) MAP solution and posterior PDF of litho-fluid facies provided by the SL algorithm for the synthetic inversion of the seismic data derived from well A, respectively. Note the close match between the actual and the predicted profiles.

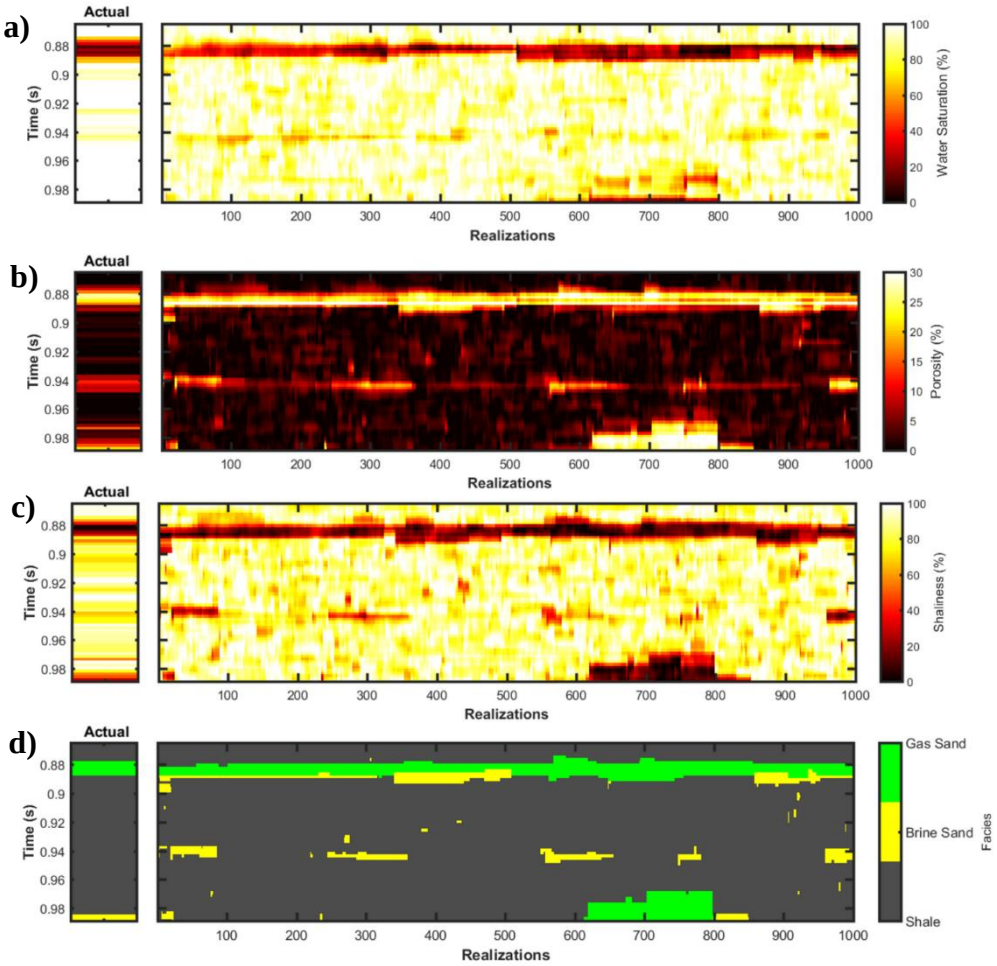

Figure 14: Comparison between the actual petrophysical properties and litho-fluid facies with the realizations of the SL algorithm for the inversion of the synthetic seismic data pertaining to well A. a), b), c) And d) pertain to the water saturation, porosity, shaliness and litho-fluid facies.

The very similar MAP solutions achieved by the TS and SL algorithms (Figure 9, Figure 10, Figure 12, and Figure 13) seem to confirm the applicability of the two-step method for the investigate reservoir area. We now extend this comparison to the field data inversion.

Inversion of field data

We run the two implemented algorithms as part of appraisal studies of a gas-field located onshore, where seismic data were acquired with a maximum offset of 6 Km and processed following a true amplitude processing-sequence. The dominant frequency of the available seismic data is around 45-50 Hz. Angle gathers derived from time-migrated CMPs are the inputs for the two

implemented inversion algorithms. As previously discussed, borehole logs provide seismic velocities, density and petrophysical information needed to compute all the a-priori information and to derive the rock-physic models for the target zone. The information brought by these wells has been also used to validate the inversion results, while well A was used for a blind test.

Figure 15 represents a close-up of a stack section extracted from the 3D seismic volume along an in-line direction. Note the high-amplitude reflector associated with the top of the reservoir.

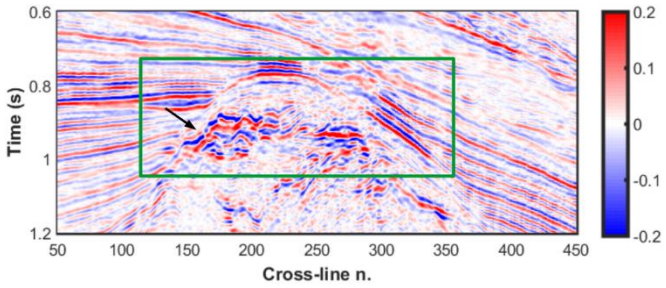

Figure 15: Example of stack section along an in-line direction extracted from the 3D seismic volume. The green rectangle delimits the target zone, while the black arrow points toward the top reflections of the reservoir.

Figure 16 illustrate the $p(\mathbf{r}|\mathbf{d})$ provided by the TS algorithm for the inversion of the CMP gathers closest to well A. First of all, note that due to the limited depth at which the reservoir is located, the first utilizable incidence angle was 15 degrees, and that only 4 seismic traces (pertaining to the incidence angles of 15-20-25-30 degrees) have been considered in the inversion. However, we observe that, although with higher uncertainties (that is broader posterior PDFs) with respect to the synthetic tests, the inversion provides MAP solutions that correctly capture the variability in the logs. In particular, note that the true properties are usually contained in the range of admissible solutions defined by the posterior PDFs. In addition, Figure 16a confirms the conclusion drawn from the Monte Carlo simulations of the expected AVA responses (Figure 5). Indeed, note that the shale-sand reflections are characterized by negligible variations of the seismic amplitudes as the

incidence angle increases. The predicted facies profiles (Figure 17) confirms the reliability of the inversion results.

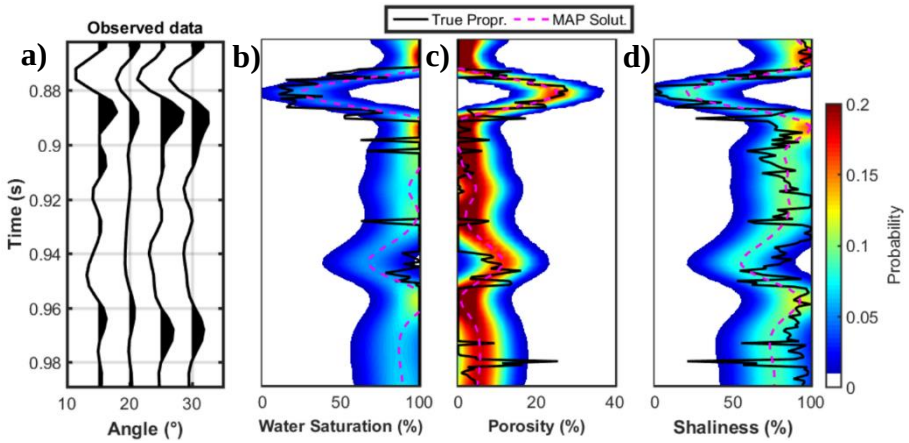

Figure 16: Inversion results provided by the TS algorithm for a field CMP gather located in correspondence of well A. a), b) c) And d) represent the observed CMP gather, and the posterior PDFs for the petrophysical properties of water saturation, porosity and shaliness, respectively. The continuous black and dashed magenta lines shown the logged properties values and the MAP solution, respectively.

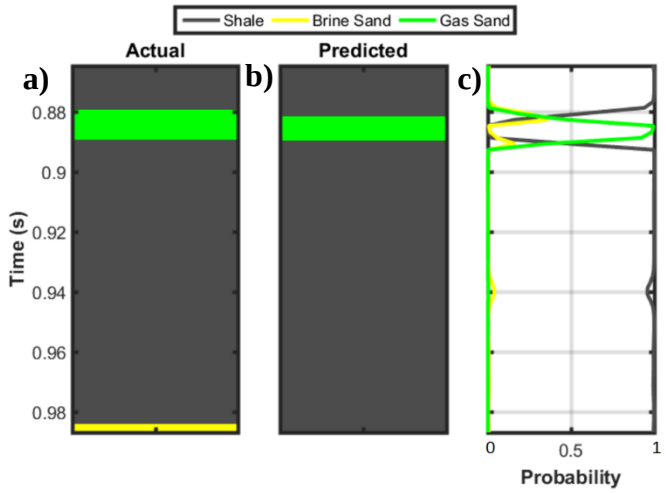

Figure 17: a) Actual facies profile at well A. b) and c) MAP solution and posterior PDF of litho-fluid facies provided by the TS algorithm for the inversion of the CMP gather located in correspondence of well A, respectively. Note the match between the actual and the predicted profiles.

Figure 18 and Figure 19 display the $p(\mathbf{r}|\mathbf{d})$ and $p(\mathbf{f}|\mathbf{d})$ estimated by the SL inversion algorithm. Again, we observe a satisfactory match between the MAP solutions and the well log information. In particular, note that with respect to the TS approach, the exact Zoeppritz equations used by the SL method as forward modelling engine, allows us to slightly extend the angle range considered in the inversion up to a maximum incidence angle of 40 degrees (Figure 18a).

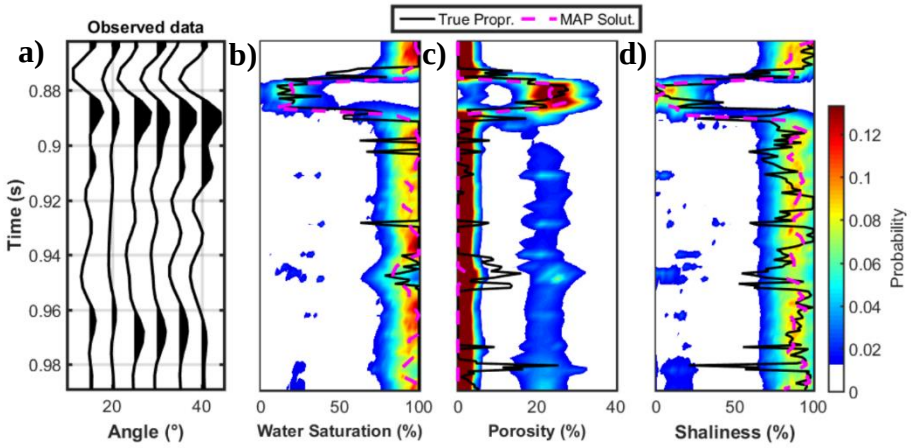

Figure 18: Inversion results provided by the SL algorithm for a field CMP gather located in correspondence of well A. a), b) c) and d) represent the observed CMP gather, and the posterior PDFs for the petrophysical properties of water saturation, porosity and shaliness, respectively. The continuous black and dashed magenta lines show the logged properties values and the MAP solution, respectively.

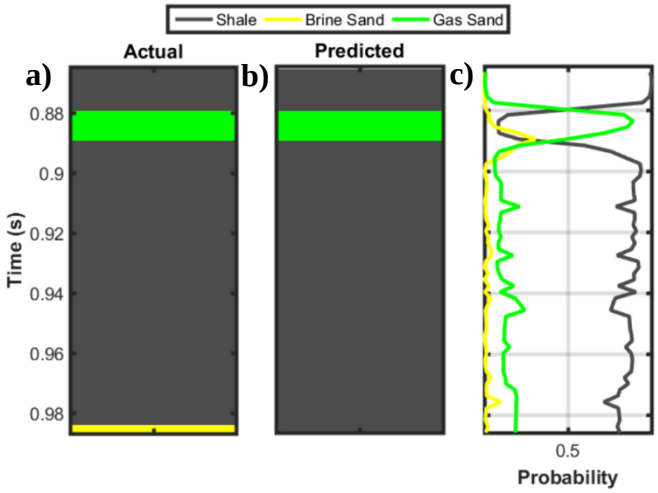

Figure 19: a) Actual facies profile at well A. b) and c) MAP solution and posterior PDF provided by the SL algorithm for the inversion of the CMP gather located in correspondence of well A, respectively. Note the close match between the actual and the predicted profiles.

In all the inversion tests we observe that, as expected, the uncertainty on the estimated petrophysical properties increase passing from porosity to shaliness and to water saturation. As previously discussed, this fact can be related to the different influence of the petrophysical properties in determining the elastic properties, and thus the seismic response. Analogously to the synthetic tests, the very similar MAP solutions yielded by the TS and SL algorithms confirm the applicability of the two-step method for reservoir characterization in the investigated area.

To more quantitatively compare the posterior PDFs estimated in the field data inversion by the TS and the SL algorithm, we compute the coverage probability for all the field seismic gathers for which well control was available to validate the results. The coverage probability is the actual probability that the considered interval (in the following the 0.80 probability interval) contains the true property value. In Table 1 note that, although the similarity between the MAP solutions estimated by the two methods, the SL algorithm provides slightly superior prediction intervals compared to the TS method. This proves that accounting for the dependence of the petrophysical properties on the litho-fluid facies can produce a more accurate description of the uncertainties affecting the estimated parameters.

	TS method	SL method
Water Saturation	0.75	0.79
Porosity	0.87	0.90
Shaliness	0.84	0.85

Table 1: The coverage probability (0.80) computed by considering the inversion results obtained for the inversion of the seismic gathers for which well control was available to validate the results.

Figure 20 and Figure 21 show the MAP solutions for petrophysical properties estimated by the TS and SL algorithms, respectively, along the in-line section and within the green rectangle represented in Figure 15. Note the high porosity and low water saturation and shaliness values that characterize the target interval located around 0.95 s and between cross-lines 150-200. Again, note the similarity between the predictions provided by the two methods along the entire section, and particularly around the target interval. The more scattered predictions visible in Figure 21 with respect to Figure 20, can be ascribed to the multimodality of the posterior PDF $p(\mathbf{r}|\mathbf{d})$ estimated by the SL algorithm. Figure 22 compares the MAP solution of litho-fluid facies classification estimated by the two methods. The considerations are similar to those drawn from Figure 20 and Figure 21. Note the prediction of gas saturated sands around the target interval.

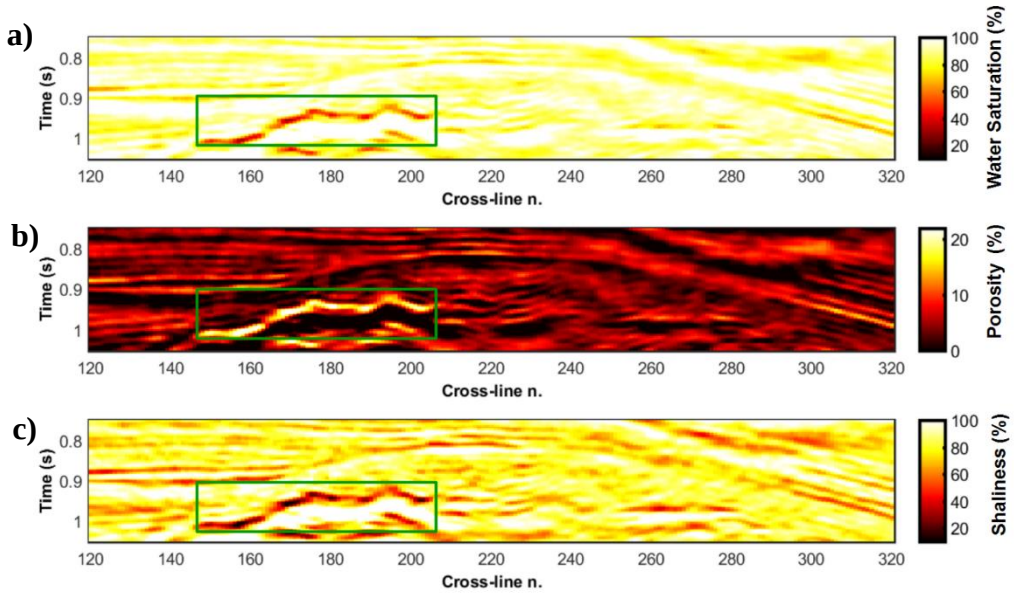

Figure 20: MAP solution of the petrophysical properties estimated by the TS algorithms along the in-line section and within the green rectangle represented in Figure 15. a), b) And c) refer to water saturation, porosity and shaliness, respectively. Note the decrease of water saturation and shaliness and the increase of porosity occurring at the target layer located around 0.95 TWT and between cross-lines 145-210 (green rectangles).

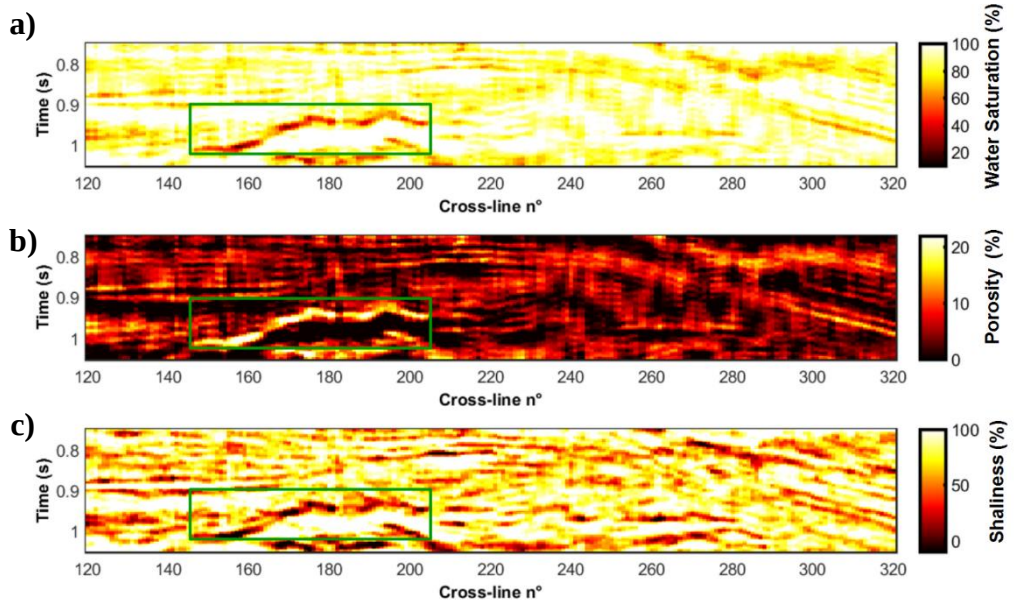

Figure 21: As in Figure 20 but for the SL algorithm.

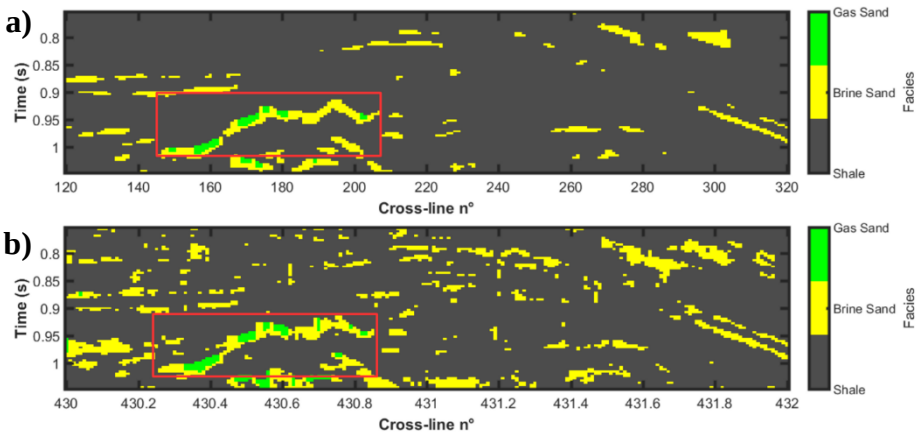

Figure 22: MAP solutions for the litho-fluid facies estimated by the TS and SL algorithms (parts a) and b), respectively) along the in-line section and within the green rectangle represented in Figure 15. Note the fair match between part a) and b) and the prevalence of gas sands in correspondence of the target layer located around 0.95 TWT and between cross-lines 145-210 (red rectangles).

Discussion

The implemented TS approach constitutes a very fast inversion algorithm that adopts an analytical Bayesian formulation under Gaussian assumption for the petrophysical parameter. This method being based on a petrophysical reformulation of a time-continuous linearization of the exact Zoepprtiz equations, is obviously limited to be applied to a narrow range of incidence angle (i.e 0-30 degrees) and under the assumption of weak elastic contrasts at the reflecting interfaces. This algorithm is based on a linear RPM; however, rock-physics models are generally non-linear, but the nonlinearity is often not strong as in the reservoir zone considered in this work. In this context, the main advantage is that the linear RPM allows us to derive analytical solutions of the petrophysical inverse problem. In addition, for slightly non-linear RPMs (i.e Raymer model, stiff sand model, inclusion model) the TS inversion can be implemented by using a local linearization of the RPM based on a truncated Taylor series and an analytical derivation of the Jacobian matrix (Grana 2016). If the rock-physics model is strongly non-linear the TS method cannot be applied, and a numerical

evaluation of the posterior PDF is required. Obviously, if needed, the TS approach can be extended to other parameterizations of the elastic forward operator: such as parameterizations in terms of seismic impedances, Lamé parameters, Poisson ratio and so on. Similarly, other rock and fluid properties, such as oil saturation and/or calcite volume, can be estimated as long as suitable rock-physics models are available. As previously discussed the TS algorithm, in its actual implementation, assumes Gaussian distributed petrophysical properties but petrophysical properties are generally not Gaussian. Grana and Della Rossa (2010) and Rimstad and Omre (2010) presented analytical formulations of the Bayesian approach for multimodal and skewed PDFs, respectively. These formulations could be used in the petrophysical inversion but they will increase the computational effort. From the one hand, the more realistic Gaussian mixture PDF provides slightly superior prediction intervals compared with the Gaussian assumption. From the other hand, the Gaussian assumption, although neglecting the facies dependent characteristics of petrophysical properties, not only simplifies the practical implementation of the inversion method, but makes it also possible to implement a fast and analytic inversion procedure that yields final estimates that can correctly capture the variability in the logs.

The SL algorithm being based on a MCMC method, provides a highly computer intensive inversion tool for an accurate uncertainty propagation. In this case, the elastic forward modelling based on the exact Zoeppritz equations makes it possible to relax the assumption of weak elastic contrasts at the reflecting interfaces and allows us to increase the angle range considered in the inversion. In addition to the GM-PDF, the SL algorithm ca be easily extended to sample different a-priori PDF of the petrophysical properties. If needed, the convolutional elastic forward modelling can be substituted with other forward operators that more realistically models the wave propagation in the subsurface (i.e. the reflectivity method). At the expense of a higher computational cost, this modification makes it possible to include multiple wave phenomena (i.e converted wave, multiple reflections) in the inversion, that might help reduce the petrophysical null-space. The SL algorithm can obviously manage linear, non-linear, empirical or theoretical RPMs, or else can be used with

different RPMs for different litho-fluid facies. Both the TS and SL inversion algorithms assume that the derived RPM calibrated at the well location is also valid far away from the well. In addition, the two methods assume bounded petrophysical properties (i.e. shaliness and water saturation bounded between 0 and 100%). For this reason, in the SL inversion, we reject any proposal that falls outside the bounds, while in the TS approach we simplistically consider the bounds as hard constrains that make the a-priori probability equal to zero outside the admissible ranges. This implies that the standard deviations of the petrophysical parameters are not representative for the whole a-priori PDF, but they are only valid for the Gaussian part (see Duijndam, 1988). However, if needed, logit transformation could be applied to transform bounded variables to variables with support in $\mathbb{R}$ (Bosch et al. 2007). For the investigated reservoir, the main difference between the TS and SL algorithm is their very different computational times. Considering a Matlab implementation and the same hardware configuration (an Intel i5 CPU @2.67 GHz), the TS method requires just a couple of hours to invert and classify the 2D section we considered, whereas the single-loop approach requires more than three days. However, the computational cost of the SL inversion can be greatly reduced by a parallel implementation in which many CMP gathers are inverted simultaneously or in which the models in each chain are sampled simultaneously. In addition to speed up the inversion procedure, the MCMC method can be substituted by the probability perturbation method (Caers et al. 2006) that seems to guarantee a faster convergence than the standard MCMC methods. A possible improvement to promote the lateral continuity of the results could be obtained by introducing spatial constrains (i.e. in the form of a variogram model) between the petrophysical properties and/or the litho-fluid facies, or else by additionally constraining the inversion results on hard data (i.e. well log data). Further work on these research topics is currently ongoing.

Conclusions

We implemented a two-step (TS) approach for seismic-reservoir characterization. In the first step, petrophysical properties are directly estimated from pre-stack seismic data by using a linear

empirical rock-physics model (RPM) and under the assumption of a Gaussian prior model. These characteristics make it possible an analytical formulation of the posterior probability density function (PDF) of petrophysical properties, and thus allowed us to implement a very fast inversion procedure. In particular, the linear RPM, specifically derived for the investigated area, was used to rewrite the time-continuous reflectivity function, which links the P-wave reflection coefficients to the elastic contrasts at the reflecting interface, in terms of petrophysical contrasts. This seismic-petrophysical forward modelling being based on a linear approximation of the exact Zoeppritz equations, limits the inversion to consider a limited range of incidence angles and to assume weak elastic contrasts at the reflecting interfaces. In the second step of litho-fluid facies identification, the posterior PDF estimated in the first step are combined with a downward Markov Chain prior model in order to estimate the posterior probability of litho-fluid facies.

To assess the reliability of the TS algorithm, we compared its predictions with those provided by a single-loop (SL) MCMC algorithm that uses the exact Zoeppritz equations as forward model, adopts a non-linear theoretical RPM, and more realistically assumes a Gaussian mixture a-priori model. From a practical point of view, the synthetic and field inversion tests proved the consistency between the MAP solutions provided by the two methods and the well log information, and demonstrated the validity of the Gaussian assumption and the suitability of the linear rock-physics model for reservoir characterization in the investigated area. The Gaussian mixture model adopted by the SL algorithm produced only a slight improvement of the description of the multimodal behavior of the final solution. In both inversions, it resulted that the porosity is the best resolved parameter, whereas the shaliness, but particularly the water saturation, are less resolvable due to their minor influence in determining the elastic parameters, and then the seismic response.

Acknowledgments

The authors wish to thank Edison for making the well log data and the seismic data available and for the permission to publish this paper. At the University of Pisa, the seismic data were processed

with the Promax software of Landmark/Halliburton who is gratefully acknowledged. We also thank the associate editor (Dr. Stéphane Operto) and four anonymous reviewers for their constructive criticism and comments that helped to significantly improve the quality of the original manuscript. We finally thank Prof. Alfredo Mazzotti for his useful suggestions.

References

Agostinetti, N.P., and A. Malinverno, 2010, Receiver function inversion by trans-dimensional Monte Carlo sampling: Geophysical Journal International, 181(2), 858-872.

Aleardi, M., A. Tognarelli, and A. Mazzotti, 2016, Characterisation of shallow marine sediments using high-resolution velocity analysis and genetic-algorithm-driven 1D elastic full-waveform inversion: Near Surface Geophysics, 14(5), 449-460.

Aleardi, M., and A. Tognarelli, 2016, The limits of narrow and wide-angle AVA inversions for high Vp/Vs ratios: An application to elastic seabed characterization: Journal of Applied Geophysics, 131, 54-68.

Aleardi, M., F. Ciabarri, and A. Mazzotti, 2017a, Probabilistic estimation of reservoir properties by means of wide-angle AVA inversion and a petrophysical reformulation of the Zoeppritz equations: Submitted to Journal of Applied Geophysics. Under review.

Aleardi, M., F. Ciabarri, T. Gukov, M. Giussani, and A. Mazzotti, 2017b, A single-step Bayesian petrophysical inversion algorithm based on a petrophysical reformulation of the P-wave reflection coefficients: In 79th EAGE Conference and Exhibition, Paris, France. Doi: 10.3997/2214-4609.201700902

Aleardi, M., and F. Ciabarri, 2017a, Assessment of different approaches to rock-physics modeling: A case study from offshore Nile Delta: Geophysics, 82(1), MR15-MR25.

Aleardi, M., and F. Ciabarri, 2017b, Application of different classification methods for litho-fluid facies prediction: A case study from offshore Nile Delta: Journal of Geophysics and Engineering, 14, 1087.

Aleardi, M., and A. Mazzotti, 2017, 1D elastic full-waveform inversion and uncertainty estimation by means of a hybrid genetic algorithm-gibbs sampler approach: Geophysical Prospecting, 65(1), 64-85.

Aleardi, M., and A. Mazzotti, 2014, A feasibility study on the expected seismic AVA signatures of deep fractured geothermal reservoirs in an intrusive basement: Journal of Geophysics and Engineering, 11(6), 065008.

Aleardi, M., A. Mazzotti, A. Tognarelli, S. Ciuffi, and M. Casini, 2015, Seismic and well log characterization of fractures for geothermal exploration in hard rocks: Geophysical Journal International, 203(1), 270-283.

Alpak, F.O., C. Torres-Verdín, and T.M. Habashy, 2006, Petrophysical inversion of borehole array-induction logs: Part I—Numerical examples: Geophysics, 71(4), F101-F119.

Amaliksen, I., 2014, Bayesian inversion of time-lapse seismic data using bimodal prior models: Masters thesis, Norwegian University of Science and Technology

Aster, R.C., B. Borchers, and C.H. Thurber, 2011, Parameter Estimation and Inverse Problem: Elsevier.

Avseth, P., T. Mukerji, and G. Mavko, 2005, Quantitative seismic interpretation. Applying rock physics tools to reduce interpretation risk: Cambridge University Press.

Bachrach, R., M. Beller, C.C. Liu, J. Perdomo, D. Shelander, N. Dutta, and M. Benabentos, 2004, Combining rock physics analysis, full waveform prestack inversion and high-resolution

seismic interpretation to map lithology units in deep water: A Gulf of Mexico case study: The Leading Edge, 23(4), 378-383.

Bongajum, E.L., J. Boisvert, and M.D. Sacchi, 2013, Bayesian linearized seismic inversion with locally varying spatial anisotropy: Journal of Applied Geophysics, 88, 31-41.

Bosch, M., 2004, The optimization approach to lithological tomography: Combining seismic data and petrophysics for porosity prediction: Geophysics, 69(5), 1272-1282.

Bosch, M., L. Cara, J. Rodrigues, A. Navarro, and M. Díaz, 2007, A Monte Carlo approach to the joint estimation of reservoir and elastic parameters from seismic amplitudes: Geophysics, 72(6), O29-O39.

Bosch, M., T. Mukerji, E.F. and Gonzalez, E., 2010, Seismic inversion for reservoir properties combining statistical rock physics and geostatistics: A review: Geophysics, 75(5), 165–176.

Buland, A., and H. Omre, 2003, Bayesian linearized AVO inversion: Geophysics, 68(1), 185-198.

Caers, J., and T.B. Hoffman, 2006, The probability perturbation method: A new look at Bayesian inverse modeling: Mathematical Geology, 38, no. 1, 81–100.

Castagna, J.P., and H.W. Swan, 1997, Principles of AVO crossplotting: The leading edge, 16(4), 337-344.

Chiappa, F., and A. Mazzotti, 2009, Estimation of petrophysical parameters by linearized inversion of angle domain pre-stack data: Geophysical Prospecting, 57(3), 413-426.

Doyen, P., 2007, Seismic Reservoir Characterization: EAGE.

Duijndam, A.J.W., 1988, Bayesian estimation in seismic inversion. Part I: Principles. Geophysical Prospecting: 36(8), 878-898.

Eidsvik, J., P. Avseth, H. Omre, T. Mukerji, and G. Mavko, 2004, Stochastic reservoir characterization using prestack seismic data: Geophysics, 69(4), 978-993.

Fernandez Martinez, J.L., M.Z Fernandez Muniz, and M.J. Tompkins, 2012, On the topography of the cost functional in linear and nonlinear inverse problems: Geophysics, 77(1), W1-W15.

Gelman A., J.B Carlin, H.S. Stern, D.B. Dunson, A. Vehtari, and D.B. Rubin, 2013, Bayesian Data Analysis: CRC Press.

Gong, T., and G.A. McMechan, 2016, Target-oriented linear least squares and nonlinear, trust-region Newton inversions of plane waves using AVA and PVA data for elastic model parameters: Geophysics, 81(5), R325-R338.

Grana, D., and E. Della Rossa, 2010, Probabilistic petrophysical-properties estimation integrating statistical rock physics with seismic inversion: Geophysics, 75(3), O21-O37.

Grana, D., T. Mukerji, J. Dvorkin, and G. Mavko, 2012, Stochastic inversion of facies from seismic data based on sequential simulations and probability perturbation method: Geophysics, 77(4), M53-M72.

Grana, D., 2016, Bayesian linearized rock-physics inversion: Geophysics, 81(6), D625-D641.

Grana, D., T. Fjeldstad, and H. Omre, 2017, Bayesian Gaussian Mixture Linear Inversion for Geophysical Inverse Problems. Mathematical Geosciences, 49(4), 493-515.

Gouveia, W.P., J.A. and Scales, 1998, Bayesian seismic waveform inversion: Parameter estimation and uncertainty analysis: Journal of Geophysical Research: Solid Earth, 103(B2), 2759-2779.

Gunning, J., and M.E. Glinsky, 2007, Detection of reservoir quality using Bayesian seismic inversion: Geophysics, 72(3), R37-R49.

Hastie, T., R. Tibshirani, and J. Friedman, 2002, The elements of statistical learning: Springer.

Hastings, W.K., 1970, Monte Carlo sampling methods using Markov chains and their applications: Biometrika, 57(1), 97-109.

Jalalalhosseini, S. M., H. Ali, and M. Mostafazadeh, 2014, Predicting Porosity by Using Seismic Multi-Attributes and Well Data and Combining These Available Data by Geostatistical Methods in a South Iranian Oil Field: Petroleum Science and Technology, 32(1), 29-37.

Larsen, A.L., M. Ulvmoen, H. Omre, and A. Buland, 2006, Bayesian lithology/fluid prediction and simulation on the basis of a Markov-chain prior model, Geophysics, 71(5), R69-R78.

Li, D., and F. Zhang, 2015, Direct Estimation of Petrophysical Properties Based on AVO Inversion: 85th Annual International Meeting, SEG, Expanded Abstracts, 2886-2890.

Mavko, G., T. Mukerji, and J. Dvorkin, 2009, The rock physics handbook: Tools for seismic analysis of porous media: Cambridge university press.

Mazzotti, A., and E. Zamboni, 2003, Petrophysical inversion of AVA data: Geophysical Prospecting, 51, 517-530.

Mosegaard, K., and A. Tarantola, 1995, Monte Carlo sampling of solutions to inverse problems. Journal of Geophysical Research: Solid Earth, 100(B7), 12431-12447.

Mosegaard, K., (2006). Monte Carlo analysis of inverse problem. PhD thesis, Copenhagen University.

Rimstad, K., and H. Omre, 2010, Impact of rock-physics depth trends and Markov random fields on hierarchical Bayesian lithology/fluid prediction: Geophysics, 75(4), R93-R108.

Sajeva, A., M. Aleardi, E. Stucchi, N. Bienati, and A. Mazzotti, 2016, Estimation of acoustic macro models using a genetic full-waveform inversion: Applications to the Marmousi model: Geophysics, 81(4), R173-R184.

Sajeva, A., M. Aleardi, B. Galuzzi, E. Stucchi, E. Spadavecchia, and A. Mazzotti, 2017a, Comparing the performances of four stochastic optimisation methods using analytic objective functions, 1D elastic full-waveform inversion and residual static computation: Geophysical Prospecting, in Print. Doi: 10.1111/1365-2478.12532

Sajeva, A., M. Aleardi, and A. Mazzotti, 2017b, Genetic algorithm full-waveform inversion, uncertainty estimation and validation of the results: Accepted for publication in Bollettino di Geofisica Teorica ed Applicata. In print. Doi. 10.4430/bgta0199.

Sambridge, M., and K. Mosegaard, 2002, Monte Carlo methods in geophysical inverse problems: Reviews of Geophysics, 40(3).

Sambridge, M., 1999, Geophysical inversion with a neighbourhood algorithm—II. Appraising the ensemble: Geophysical Journal International, 138(3), 727-746.

Sauvageau, M, E. Gloaguen, M. Claprood, R. Lefebvre, and M. Bêche, 2014, Multimodal reservoir porosity simulation: an application to a tight oil reservoir: Journal of Applied Geophysics, 107, 71-79.

Sen, M.K., and P.L. Stoffa, 1996, Bayesian inference, Gibbs' sampler and uncertainty estimation in geophysical inversion: Geophysical Prospecting, 44(2), 313-350.

Shahraeeni, M.S., and A. Curtis, 2011, Fast probabilistic nonlinear petrophysical inversion: Geophysics, 76(2), E45-E58.

Skopintseva, L., A. Aizenberg, M. Ayzenberg, M. Landrø, and T. Nefedkina, 2012, The effect of interface curvature on AVO inversion of near-critical and postcritical PP-reflections: Geophysics, 77(5), N1-N16.

Stolt, R.H., and A.B. Weglein, 1985, Migration and inversion of seismic data. Geophysics, 50(12), 2458-2472.

Tarantola, A. (2005). Inverse problem theory and methods for model parameter estimation. Siam, 2005.

Ulvmoen, M., and H. Omre, 2010, Improved resolution in Bayesian lithology/fluid inversion from prestack seismic data and well observations: Part 1—Methodology: Geophysics, 75(2), R21-R35.

Veire, H.H., H.G. Borgos, and M. Landrø, 2006, Stochastic inversion of pressure and saturation changes from time-lapse AVO data: Geophysics, 71(5), C81-C92.

Zunino, A., K. Mosegaard, K. Lange, Y. Melnikova, and T. Mejer Hansen, 2014, Monte Carlo reservoir analysis combining seismic reflection data and informed priors: Geophysics, 80(1), R31-R41.

Figure captions

Figure 1: Comparison between logged elastic properties (black curves) and predicted properties by the empirical RPM (red curves) and by the theoretical RPM (green dashed curves). a), b) And c) refer to ln(density), ln(Vp) and ln(Vs), respectively. Note the very similar predictions given by the empirical and the theoretical RPMs. For the empirical RPM the resulting correlation coefficients are 0.94, 0.91 and 0.81 for density, Vp, and Vs respectively. For the theoretical RPM the resulting correlation coefficients are 0.94, 0.93 and 0.82 for density, Vp, and Vs respectively.

Figure 2: Comparison between actual and predicted RPTs by the empirical RPM of equation 38.1-3. a) RPTs derived from actual well log data and showing the influence of each petrophysical parameter on the natural logarithm of the P-impedance (Ip) and S-impedance (Is) values. The influence of water saturation, porosity and shaliness is represented from top to bottom. b) RPTs predicted by the empirical RPM. Note that the main trends visible in a) are well predicted by the estimated RPM.

Figure 3: The error PDF $p_{TS}(\boldsymbol{\varepsilon})$ for the empirical RPM (f^{1}_{RPM}) that expresses the variability of elastic properties that is not described by the estimated rock-physics model. The black dots show the difference between the natural logarithm of actual and predicted Ip and Is values, whereas the colored contours represent the Gaussian PDF derived on the ensemble of black dots (blue and red colors code low and high probabilities, respectively).

Figure 4: a) and b) Cross-plots showing the distribution of the natural logarithm of P-wave, S-wave velocities and density within each facies. The data have been extracted from the available well log data around the reservoir interval. Gray, yellow and green colors refer to shale, brine sand and gas sand, respectively. Note the decreases of density and Vp when moving from shale, to brine

sand, and to gas sand and also the very similar S-wave velocity values within the three litho-fluid facies.

Figure 5: The expected PDFs of AVA responses in the target zone computed for a shale-shale contact (a), a shale-brine sand contact (b), and a shale-gas sand contact (c). In all cases note the limited variations of the reflected amplitudes as the incidence angle increases.

Figure 6: The expected PDF of the intercept and gradient values for the shale-shale, shale-brine sand and shale-gas sand reflecting interfaces.

Figure 7: Comparison between synthetic CMP gathers obtained from well A by using an elastic forward modelling (equation 7) and a petrophysical forward modelling (equation 15) that was derived by incorporating the empirical RPM of equation 38.1-3 in the time-continuous approximation of the P-wave reflection coefficients. The negligible differences between the seismic data obtained by the two different forward modelling parameterizations, demonstrate the reliability of the derived linear RPM. For a better comparison, all the seismograms are represented with the same amplitude normalization.

Figure 8: a), b) and c) Posterior PDFs for water saturation, porosity and shaliness estimated by the TS method when the logged elastic properties of Vp, Vs and density of well A are inverted. The match between the true properties values (continuous black lines) and the MAP solutions (dashed magenta lines) confirms the reliability of the empirical RPM of equation 38.1-3 and its suitability for reservoir characterization in the investigated area. Note the increase of uncertainties when passing from porosity, to shaliness and to water saturation.

Figure 9: Inversion results provided by the TS algorithms for a synthetic CMP gather pertaining to well A. a), b) c) And d) represent the observed CMP gather, and the posterior PDFs for the petrophysical properties of water saturation, porosity and shaliness, respectively. The continuous black and dashed magenta lines display the logged property values and the MAP solution, respectively. Note that, although with a lower vertical resolution, the MAP solutions closely match the actual property values.

Figure 10: a) Actual facies profile at well A. b) And c) MAP solution and posterior PDF of litho-fluid facies provided by the TS algorithm for the synthetic inversion of the seismic data derived from well A, respectively. Note the close match between the actual and the predicted profiles.

Figure 11: Comparison of prior and posterior PDFs of litho-fluid facies and petrophysical properties, derived by imposing in the SL inversion a likelihood value equal to one. a), b), c) And d) represent the PDFs of litho-fluid facies, water saturation, porosity and shaliness, respectively. The close match between prior and posterior PDFs proves that the distribution of the proposed models exactly follows the prior PDF.

Figure 12: Inversion results provided by the SL algorithms for the synthetic CMP gather pertaining to well A. a), b) c) And d) represent the observed CMP gather, and the posterior PDFs for the petrophysical properties of water saturation, porosity and shaliness, respectively. The continuous black and dashed magenta lines display the logged property values and the MAP solution, respectively. Note that, although with a lower vertical resolution, the MAP solutions closely match the true property values.

Figure 13: a) Actual facies profile at well A. b) and c) MAP solution and posterior PDF of litho-fluid facies provided by the SL algorithm for the synthetic inversion of the seismic data derived from well A, respectively. Note the close match between the actual and the predicted profiles.

Figure 14: Comparison between the actual petrophysical properties and litho-fluid facies with the realizations of the SL algorithm for the inversion of the synthetic seismic data pertaining to well A. a), b), c) And d) pertain to the water saturation, porosity, shaliness and litho-fluid facies.

Figure 15: Example of stack section along an in-line direction extracted from the 3D seismic volume. The green rectangle delimits the target zone, while the black arrow points toward the top reflections of the reservoir.

Figure 16: Inversion results provided by the TS algorithm for a field CMP gather located in correspondence of well A. a), b) c) And d) represent the observed CMP gather, and the posterior PDFs for the petrophysical properties of water saturation, porosity and shaliness, respectively. The continuous black and dashed magenta lines shown the logged properties values and the MAP solution, respectively.

Figure 1723: a) Actual facies profile at well A. b) and c) MAP solution and posterior PDF of litho-fluid facies provided by the TS algorithm for the inversion of the CMP gather located in correspondence of well A, respectively. Note the match between the actual and the predicted profiles.

Figure 18: Inversion results provided by the SL algorithm for a field CMP gather located in correspondence of well A. a), b) c) and d) represent the observed CMP gather, and the posterior PDFs for the petrophysical properties of water saturation, porosity and shaliness, respectively. The

continuous black and dashed magenta lines show the logged properties values and the MAP solution, respectively.

Figure 19: a) Actual facies profile at well A. b) and c) MAP solution and posterior PDF provided by the SL algorithm for the inversion of the CMP gather located in correspondence of well A, respectively. Note the close match between the actual and the predicted profiles.

Table 1: The coverage probability (0.80) computed by considering the inversion results obtained for the inversion of the seismic gathers for which well control was available to validate the results.

Figure 20: MAP solution of the petrophysical properties estimated by the TS algorithms along the in-line section and within the green rectangle represented in Figure 15. a), b) And c) refer to water saturation, porosity and shaliness, respectively. Note the decrease of water saturation and shaliness and the increase of porosity occurring at the target layer located around 0.95 TWT and between cross-lines 145-210 (green rectangles).

Figure 21: As in Figure 20 but for the SL algorithm.

Figure 22: MAP solutions for the litho-fluid facies estimated by the TS and SL algorithms (parts a) and b), respectively) along the in-line section and within the green rectangle represented in Figure 15. Note the fair match between part a) and b) and the prevalence of gas sands in correspondence of the target layer located around 0.95 TWT and between cross-lines 145-210 (red rectangles).